Report Title:	**Geomechanical Simulation of Fluid-Driven Fractures**
Type of Report:	**Final Scientific/Technical Report**
Start Date:	**December 1, 2009**
End Date:	**November 30, 2012**
Principal Authors:	**R. Makhnenko, D. Nikolskiy, S. Mogilevskaya, J. Labuz**
Date Report:	**February 2013**
DOE Award:	**DE-FE0002020**
Submitting:	**University of Minnesota**
	200 Oak Street SE, Suite 450
	Minneapolis, MN 55455-2070

DISCLAIMER

ABSTRACT

The project supported graduate students working on experimental and numerical modeling of rock fracture, with the following objectives: (a) perform laboratory testing of fluid-saturated rock; (b) develop predictive models for simulation of fracture; and (c) establish educational frameworks for geologic sequestration issues related to rock fracture. These objectives were achieved through (i) using a novel apparatus to produce faulting in a fluid-saturated rock; (ii) modeling fracture with a boundary element method; and (iii) developing curricula for training geoengineers in experimental mechanics, numerical modeling of fracture, and poroelasticity.

TABLE OF CONTENTS

EXECUTIVE SUMMARY

Carbon storage technologies offer a means of reducing CO_2 emissions and mitigating climate change. These new technologies will require a workforce educated in geomechanics. To this end, the project supported graduate students working on geomechanical simulation of fluid-driven fractures with the following objectives:

1. Measure elastic and inelastic response of fluid-saturated rock
2. Develop predictive models for simulation of fluid-driven fractures

1. Deformation and damage of a porous, fluid-saturated rock under drained and undrained conditions were investigated. A plane-strain apparatus was modified in order to conduct tests with water-saturated rock specimens and to measure the pore pressure within the rock. Transducers within the apparatus were calibrated at the various loading states and the compliances of the system were determined. Plane strain compression and conventional triaxial compression tests were performed at different confining pressures under air-dry, drained, and undrained conditions. The behavior of the rock was evaluated within the framework of linear poroelasticity. Dilatant hardening and contractant softening was investigated from undrained experiments, where pore pressure was measured throughout the failure process. The parameters that govern the inelastic deformation of fluid-saturated rock, *i.e.* dilatancy angle β, friction coefficient μ, poroelastic coefficient K_{eff}, shear modulus G, and inelastic hardening modulus H, were calculated for the drained response. The constitutive model predicts the undrained inelastic response of the rock fairly well, almost up to the peak load if compared with the undrained test that had the same effective mean stress at the onset of inelasticity. Knowledge of dilatant hardening behavior is essential for the proper assessment of underground structures, such as long-term CO_2 storage facilities.

2. The boundary element method (BEM) is based on the boundary integral representation equivalent to the differential equation governing a specific physical problem. Such representation is possible when the so-called fundamental solution of the governing differential equation is available. The fundamental solution satisfies the differential equation everywhere in the domain except one point where it is singular. In the case of linear isotropic and homogeneous elasticity, the fundamental solution is that of a point force applied to an infinite domain, the so-called Kelvin solution. Thus, in the BEM, unlike in the finite element method (FEM), the fields are already exactly self-equilibrated inside the computational domain, perhaps except for the boundary. This makes possible resolving high stress gradients and intrinsic singularities that are difficult to handle with FEM. Another significant feature of BEM is the absence of the volume mesh, which makes it possible to solve infinite medium problems. These features of BEM make it a powerful and versatile tool for various applications. The displacement discontinuity method consists of representing a crack by a set of displacement discontinuity elements. Knowing the analytical solution for the fields for a single element, the

numerical solutions for those in the computational domain can be obtained by the standard superposition. Mathematically, this method is equivalent to the solution of a hypersingular integral equation with displacement discontinuity being the unknown density function. This approach requires a rigorous treatment of hypersingular integrals. BEM provides stable results even with the simplest piecewise-constant approximations of unknowns. However, to improve accuracy, large numbers of elements are required and, consequently, the computational cost could be high. To reduce this cost, quadratic approximations of unknowns are planned to be introduced. In this procedure, analytical integration can still be used. In fact, all integral terms involved in the present (constant approximation) scheme will still be included in the final expressions for quadratic approximations. Additional integrals related to the higher order terms are expected to be handled analytically.

INTRODUCTION

The characterization of elastically and inelastically deforming rock under well-controlled drainage conditions is required in order to understand the coupling between rock deformation and pore fluid diffusion, and for the interpretation of premonitory events in the Earth's crust prior to faulting (*e.g.* Nur 1972; Scholz *et al.* 1973; Rice and Cleary 1976). This consideration is particularly important when analyzing the stability of long-term underground storage facilities, such as the storage of CO_2.

Terzaghi (1936) was one of the first to recognize the role of the pore pressure in soil and he suggested the "effective" stress law: the effect of the pore fluid on some aspect of the mechanical behavior can be incorporated by replacing the normal stress by the effective normal stress, the difference between the normal stress and pore fluid pressure. Terzaghi's empirical expression turns out to be very good description for soil, and nearly correct for highly porous and cracked rock, but it is not true as a general rule for all porous media.

Biot (1941) developed the first rational theory for the mechanical behavior of porous materials, and later (Biot 1973) extended *poroelasticity* to the case of nonlinear behavior. Based on Biot's work, Nur and Byerlee (1971) rederived the expression for the effective stress by multiplying the pore pressure by the so-called Biot's coefficient.

The inelastic deformation of many geological materials is inhibited by an increase of hydrostatic compression, thus, an increase in pore fluid pressure decreases the effective compressive stress and promotes further inelastic deformation; conversely, a decrease in pore fluid pressure tends to inhibit further inelastic deformation (Rice 1975). Coupling of deformation with pore fluid diffusion also introduces time dependence into the response of an otherwise rate-independent solid. An elastic fluid-infiltrated solid responds more stiffly to deformations that are rapid compared to the time scale of diffusion, than for deformations that are slow compared to the diffusion time (Rice 1975; Brace and Martin 1968). However, some experimental work (Aldrich 1969) does not support this statement.

If the time scale of deformation is rapid in comparison to that for diffusion so that the fluid mass in a material element remains constant, then the response is termed "undrained." The long-time or "drained" response is the one for which the local pore fluid pressure is constant. Both elastic and inelastic material parameters differ under drained and undrained conditions (Rice and Cleary 1976; Rice 1975). Laboratory measurements that provide estimates of poroelastic parameters and consider the rate dependent effects of coupling of deformation with pore fluid diffusion are needed to describe these effects.

OBJECTIVES

The proposed study deals experiments and numerical modeling. Drained and undrained tests of porous rock were performed with the University of Minnesota Plane-Strain Apparatus, modified for this purpose. The device allowed application of three different principal stresses and measurement of principal strains, as well as the ability to apply and measure pore pressure within

the rock. Post-failure displacements and loads were measured in the plane of deformation, and friction and dilatancy characteristics of the naturally formed failure plane were determined. Moreover, eight acoustic emission (AE) sensors were used for monitoring damage in the specimen and measuring velocities.

The objective of the numerical part of the research was to develop a three-dimensional analytical and computational basis for realistic modeling of behavior of rock masses under various loading conditions and physical effects (*e.g.* fluid flow, pore pressure). The goal was to create a computational model implemented in a general purpose code capable of accurate modeling of three-dimensional problems of multiple propagating fractures in piecewise homogeneous rocks that account for various loading conditions. The code structure allowed for incorporation of coupled problems of poroelasticity. Significant features of the code include using MATLAB as the programming tool. MATLAB is a high-level language for numerical computations that features built-in linear algebra functions, graphics for data visualization, and could be easily integrated with external applications and languages.

EXPERIMENTAL METHODS

Poroelastic response

Drained and undrained material parameters can be obtained by using a compression test with pore pressure involved (Fig. 1). A barrier allows flow of the pore fluid out of the specimen during loading and, hence, constant pore pressure (drained test); the barrier prevents flow and allows pore pressure build-up (undrained test), or the equilibration of increments of pore and confining pressures (unjacketed test). Also, a dry test, when air in the pores is the only pore fluid, can be considered as the drained test (*e.g.* Green and Wang 1986; Rudnicki 1985), where the influence of the pore fluid on the rock constituents is neglected.

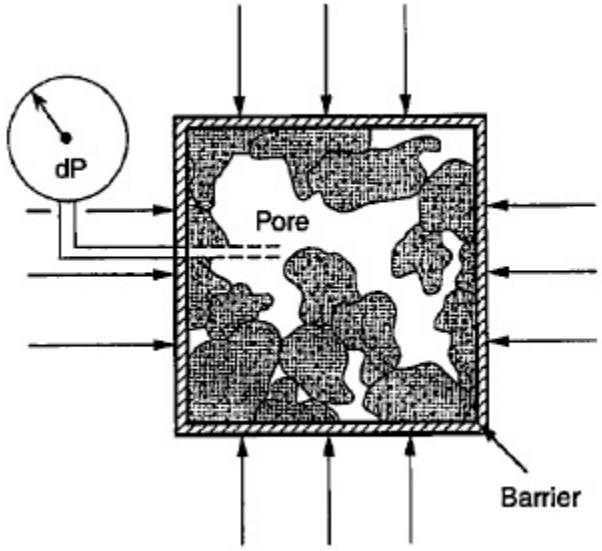

Figure 1. Rock compression with pore pressure measurements (Wang 2000).

Generalized Hooke's law for the incremental behavior of an isotropic linearly elastic solid in plane strain takes the following form for principal strains and stresses (ε_2=0):

$$\Delta\varepsilon_1 = \frac{1+\nu}{E}\left[(1-\nu)\Delta\sigma_1 - \nu\Delta\sigma_3\right]$$

$$\Delta\varepsilon_3 = \frac{1+\nu}{E}\left[(1-\nu)\Delta\sigma_3 - \nu\Delta\sigma_1\right] \quad (1)$$

$$\Delta\sigma_2 = \nu\left(\Delta\sigma_1 + \Delta\sigma_3\right)$$

Assuming constant confining pressure throughout the test ($\Delta\sigma_3$=0) and taking the sign convention of compression positive, Young's modulus E and Poisson's ratio ν are

$$E = \Delta\sigma_1 \frac{\Delta\varepsilon_1 - 2\Delta\varepsilon_3}{\left(\Delta\varepsilon_1 - \Delta\varepsilon_3\right)^2} \quad (2)$$

$$\nu = \frac{-\Delta\varepsilon_3}{\Delta\varepsilon_1 - \Delta\varepsilon_3} \quad (3)$$

For plane problems, it is convenient to introduce the invariants named (i) average stress s, (ii) shear stress τ, (iii) volume strain ε_V, and (iv) shear strain γ:

$$s = \left(\sigma_1 + \sigma_3\right)/2$$

$$\tau = \left(\sigma_1 - \sigma_3\right)/2 \quad (4)$$

$$\varepsilon_V = \varepsilon_1 + \varepsilon_3$$

$$\gamma = \varepsilon_1 - \varepsilon_3$$

Generalized Hooke's law for plane-strain becomes

$$\Delta\gamma = \frac{1}{G}\Delta\tau \quad (5)$$

$$\Delta\varepsilon_V = \frac{2(1+\nu)}{3K}\Delta s \quad (6)$$

Bulk modulus K and shear modulus G are

$$K = \frac{E}{3(1-2\nu)} \quad (7)$$

$$G = \frac{E}{2(1+\nu)} \quad (8)$$

For undrained elastic behavior in terms of total stresses, undrained Young's modulus E_u and undrained Poisson's ratio ν_u are introduced. Then, generalized Hooke's law for undrained plane-strain loading can be written in terms of equations (5) and (6), but for undrained elastic parameters:

$$\Delta\varepsilon_V = \frac{2(1+\nu_u)}{3K_u}\Delta s \quad (9)$$

$$\Delta\gamma_u = \frac{1}{G_u}\Delta\tau \quad (10)$$

where undrained bulk and shear moduli are

$$K_u = \frac{E_u}{3(1-2\nu_u)} \quad (11)$$

$$G_u = \frac{E_u}{2(1+\nu_u)} \tag{12}$$

In case of undrained testing, the pore pressure u must be considered and Terzaghi's effective stresses take the following form:

$$\begin{aligned} \sigma_1' &= \sigma_1 - u \\ \sigma_3' &= \sigma_3 - u \\ s' &= (\sigma_1' + \sigma_3')/2 \\ \tau' &= (\sigma_1' - \sigma_3')/2 = (\sigma_1 - \sigma_3)/2 = \tau \end{aligned} \tag{13}$$

Furthermore, because $\Delta\tau' = \Delta\tau$,

$$G_u = G' \tag{14}$$

where G' is the drained shear modulus, which will be denoted as G for convenience. Therefore, once ν_u and E_u are obtained from an undrained plane-strain test, other parameters such as K_u and G can be determined.

Coupling between pore pressures and external stresses in deformation of rock is described by theories of Biot (1941) and Gassman (1951). The compression of fluid-saturated rock was examined theoretically by Biot and Willis (1957), Nur and Byerlee (1971) and Brown and Korringa (1975), and experimentally by Geertsma (1957) and Fatt (1959), among others. Analyses of the problems involving interaction between fluid and rock are greatly facilitated by the work of Rice and Cleary (1976), with no special assumptions regarding the fluid and solid compressibilities. The coupled stress and fluid-flow fields are formulated as an extension of the Biot (1941) theory. The Biot moduli are written in terms of parameters related to the drained and undrained response of fluid-saturated material.

Drained and undrained bulk moduli (K and K_u) refer to boundary conditions in which there are no changes in pore fluid pressure (du=0) and pore fluid mass (dm_f=0), respectively. They can be written in terms of changes of the external mean stress P with specimen volume V:

$$K = -V \left.\frac{\partial P}{\partial V}\right|_{du=0} \tag{15}$$

$$K_u = -V \left.\frac{\partial P}{\partial V}\right|_{dm_f=0} \tag{16}$$

The Skempton coefficient B can be defined as

$$B = \left.\frac{\partial u}{\partial P}\right|_{dm_f=0} \tag{17}$$

and measured experimentally. Rice and Cleary (1976) introduced two new material constants – unjacketed (dP=du) bulk modulus K_s' and unjacketed pore volume bulk modulus K_s'':

$$K_s' = -V \left.\frac{\partial u}{\partial V}\right|_{du=dP} \tag{18}$$

$$K_s'' = -V_\phi \left.\frac{\partial u}{\partial V_\phi}\right|_{du=dP} \tag{19}$$

where $V_\phi = \phi V$ and ϕ = porosity.
The coefficients K_s' and K_s'' are two bulk moduli, which under certain conditions can be both identified with the bulk modulus K_s of the solid constituent. Assuming that the rock has fully connected pore space, all points of the solid phase may be taken as elastically isotropic with the same local bulk modulus K_s, and both fluid and solid are chemically inert for the time scale of the tests, it can be shown that (Rice and Cleary 1976):

$$K_s = K_s' = K_s'' \tag{20}$$

However, this assumption may not be valid for sedimentary rocks where intergranular cements and pore linings have different elastic properties (Green and Wang 1986).

Detournay and Cheng (1993) summarized the dependence of bulk continuum constants B, K, K_u, and α (Biot coefficient) on bulk moduli of the fluid (K_f), solid and pores:

$$\alpha = 1 - \frac{K}{K_s'}$$

$$K_u = K + \frac{\alpha^2 K}{(1-\alpha)\alpha + \phi K\left(\frac{1}{K_f} - \frac{1}{K_s''}\right)} \tag{21}$$

$$B = \frac{K_u - K}{\alpha K_u}$$

and the following inequalities must be satisfied:

$$0 < K \le K_u \tag{22}$$

$$0 < K \le K_s' \tag{23}$$

The interstitial water of a nearly saturated (S > 90%) soil is a mixture of water and gas that has a fluid bulk modulus K_f (Verruijt 1969):

$$\frac{1}{K_f} = \frac{1}{K_w} + \frac{1-S}{u} \tag{24}$$

where S is the degree of saturation, and $K_w = 2.2GPa$ is the bulk modulus of pure water. Equation (24) shows that even a small variation in the degree of saturation strongly influences the bulk modulus of the fluid. For rock, where drained testing for some reason may not be possible and only K_u is available from the undrained test (*e.g.* shale), certain assumptions $K_s = K_s' = K_s''$ and the known value of S must be made to calculate the poroelastic parameters (Makhnenko *et al.* 2011).

If both drained and undrained bulk moduli are available from the test data, then (21) has three equations and four unknowns. It can be assumed that $K_s = K_s' = K_s''$, and then α, K_s, and K_f, and hence S from equation (24), can be calculated. Also, if the assumption is made on the value of saturation S and no restrictions imposed on K_s' and K_s'', then the solution of (21) provides the values of α, K_s', and K_s''.

Plane-strain apparatus

An apparatus for determining the constitutive response of soft rock, named the University of Minnesota Plane-Strain Apparatus, was designed and built based on a passive stiff-frame concept (Labuz et al. 1996). The biaxial device (U.S. Patent 5,063,785) is unique because it allows the failure plane to develop and propagate in an unrestricted manner. By placing the upper platen on a low friction linear bearing, the prismatic specimen, subjected to confining pressure and compressed axially, has the freedom to translate in the lateral direction if the deformation has localized. In addition, the apparatus was modified to allow pore pressure to be applied and monitored during an experiment.

The design of the plane-strain apparatus is illustrated in Fig. 2; a brief explanation of the various parts of the device follows. A prismatic specimen (1) of height h = 75-100 mm, thickness t = 30-44 mm, and width w = 100 mm, is covered with an impermeable polyurethane coating to isolate the rock from the confining fluid. For the specimens to be water-saturated, a viton membrane is used to prevent polyurethane penetration into the rock. The specimen is placed on a lower loading platen (2) and confined laterally by a biaxial frame (3) in the form of a thick-walled cylinder. A pair of equally angled wedges allowing a tolerance of 0.5 mm in specimen width is used for fitting the specimen within the biaxial frame (Fig. 3). The lower loading plate is connected through a load cell (4) to the base unit (5) of the apparatus. The biaxial frame sits on the base unit guided by three pins, which ensures precise alignment. Another loading plate (6) rests on top of the specimen; it is fixed with bolts to a linear bearing (7) sliding over a trackway (8). The trackway is connected through bolts to a loading piston (9). The apparatus is placed inside a large pressure cell to induce confining (lateral) stress. The cell consists of a base pot (10), a pressure vessel (11) rated to 24 MPa, and an upper cap (12). Low friction teflon O-rings are used for sealing the loading piston and the upper caps, as well as the other connecting members of the pressure cell. The cell is filled with hydraulic oil and the confining pressure is applied with a microprocessor-based hydraulic pump that maintains cell pressure at a constant value, within a tolerance of 0.1 MPa.

The apparatus is internally instrumented with LVDTs for determining lateral and axial displacements of the specimen and movement of the linear bearing, a load cell for measuring the axial force, and strain gages for determining the plane-strain stress. The confining pressure is recorded by a pressure transducer within the hydraulic system; two pressure transducers measure the pore pressure both at the bottom and top of the specimen.

The axial force is measured below and above the specimen. A 1 MN load cell, with a sensitivity of 50 kN/mV, is mounted permanently to the cross head of the load frame and provides the axial force above the specimen. A confining pressure-compensated load cell, with a sensitivity of 5 kN/mV, is placed below the specimen, between the lower loading platen and the base unit.

Five RDP-Electrosense type D5/100/90, pressure resistant LVDTs with a linear range of 2.5 mm and a sensitivity of 0.25 mm/mV measure the displacements of the specimen and the linear bearing. Two LVDTs are attached to the lower load cell and rest against the upper loading platen for measuring axial displacement. A pair of LVDTs are placed horizontally on opposite sides of the specimen exposed to confining pressure at 5 mm above and below the specimen's mid-height for measuring lateral displacement. The four LVDTs are mounted in place through LVDT

holders attached with two aluminum posts to the lower load cell (Fig. 2). One LVDT is attached to the linear bearing to record its horizontal displacement.

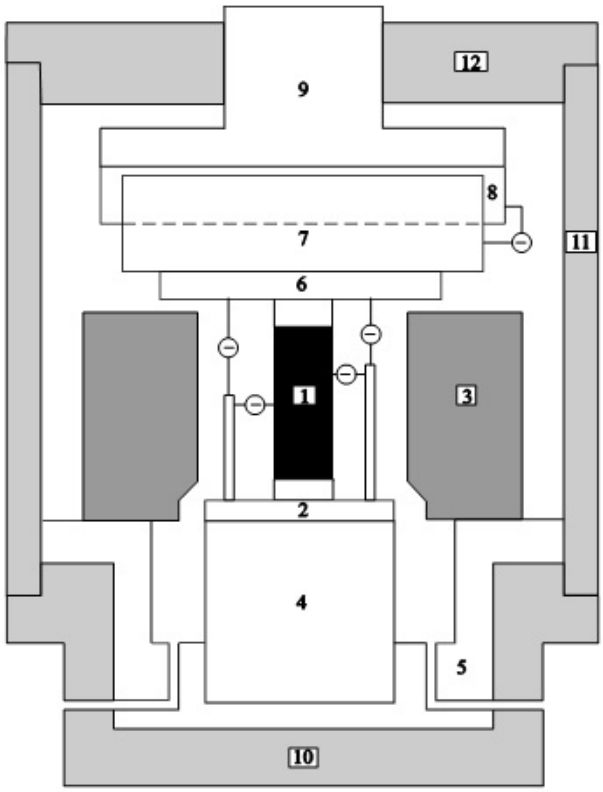

Figure 2. University of Minnesota Plane-Strain Apparatus.

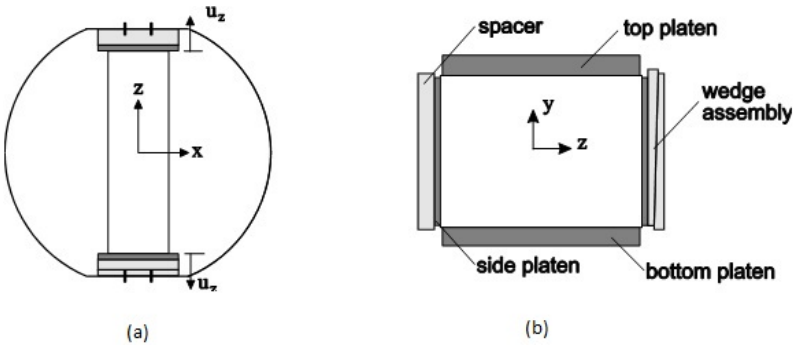

Figure 3. Specimen and wedge-spacer assembly. a. Plan view. b. Elevation view.

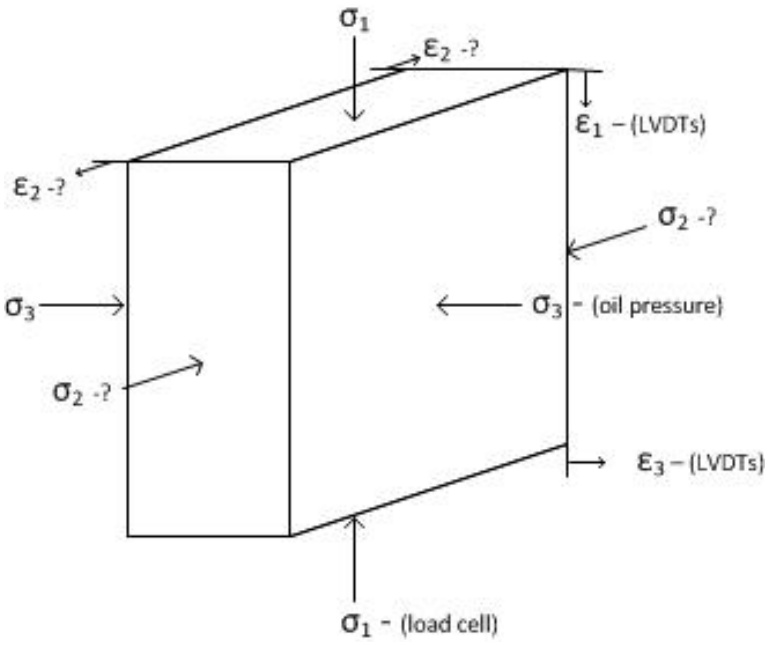

Figure 4. Principal stresses and strains.

Figure 4 illustrates principal stresses acting on the rock specimen and the corresponding strains. The direction of major principal stress σ_1 is the direction of axial loading, which is measured by the upper and lower load cells. Minor principal stress σ_3 is applied by confining fluid (hydraulic oil) and is measured by the pressure transducer in the hydraulic system. The intermediate principal stress σ_2 acts in the direction of plane strain. According to the generalized Hooke's law,

$$\sigma_2 = \varepsilon_2 E + \nu(\sigma_1 + \sigma_3) \qquad (25)$$

During the assembly, the specimen is pre-stressed in the frame with the matching wedges to guarantee $\sigma_2 > \sigma_3$.

Displacements of the specimen in major and minor principal directions are measured by the axial and lateral LVDTs. However, part of the measured displacement is related to the deformation of various components (Fig. 5), and this is called system displacement,, which is estimated from calibration tests with materials of known elastic properties such that specimen strains ε_1 and ε_3 can be accurately calculated. In addition, strain gages attached to the biaxial frame parallel to the σ_2 direction provide a measure of the specimen strain ε_2, and the intermediate principal stress is determined from eq. (25).

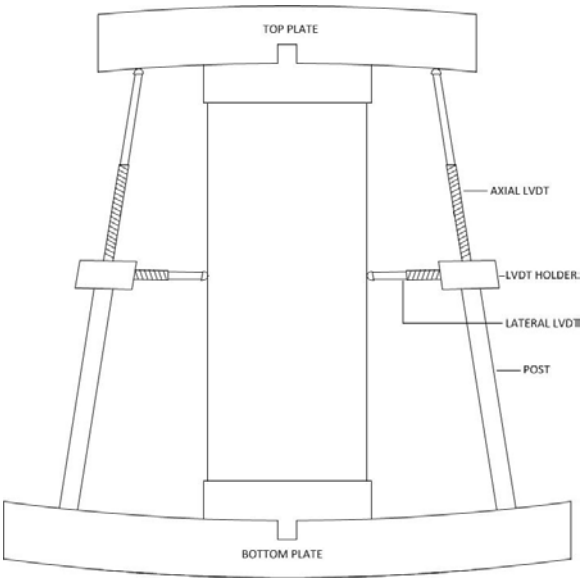

Figure 5. System displacements.

Prismatic specimens of (i) PMMA with E = 3.2 GPa, ν = 0.37, and (ii) lead with E = 15.7 GPa, ν = 0.40, similar in size to the rock specimens, were placed within the plane-strain apparatus and loaded elastically at confining pressures of 0, 5, 10, and 15 MPa.
As shown by Labuz *et al.* (1996), the frame strain is linearly proportional to ε_2 (Fig. 6):

$$\varepsilon_f = \kappa^f(\sigma_3, A)\varepsilon_2 \tag{26}$$

but the coefficient of proportionality $\kappa^f(\sigma_3,A)$ is dependent on confining pressure σ_3 and specimen size A.

The magnitude of axial system displacement u_1^{sys} is

$$u_1^{sys} = u_1^{LVDT} - \varepsilon_1^{gage} h \tag{27}$$

where u_1^{LVDT} and $\varepsilon_1^{gage} h$ are the displacement measured with the axial LVDT and the specimen displacement determined from the axial strain gage respectively. It was observed that at low axial loads, a fourth order polynomial is the best fit function to characterize the axial system compliance (Fig. 7). However, at higher loads (> 30 kN), the dependence of axial system displacement from the load F_1 becomes linear and can be written as

$$u_1^{sys} = C_A(\sigma_3, A)F_1 \tag{28}$$

where $C_A(\sigma_3,A)$ is the axial system compliance.
Lateral strain cannot be determined from strain gages, as the surfaces of a specimen parallel with the lateral LVDTs are in contact with the biaxial frame (Fig. 3). The lateral specimen strain was calculated with generalized Hooke's law:

$$\varepsilon_3 = \frac{1}{E}(\sigma_3 - \nu(\sigma_1 + \sigma_2)) \tag{29}$$

Lateral displacement of the system is the difference between the elastic lateral displacement of half of the specimen and the average displacement of two lateral LVDTs:

$$u_3^{sys} = u_3^{LVDT} - \varepsilon_3 t/2 \tag{30a}$$

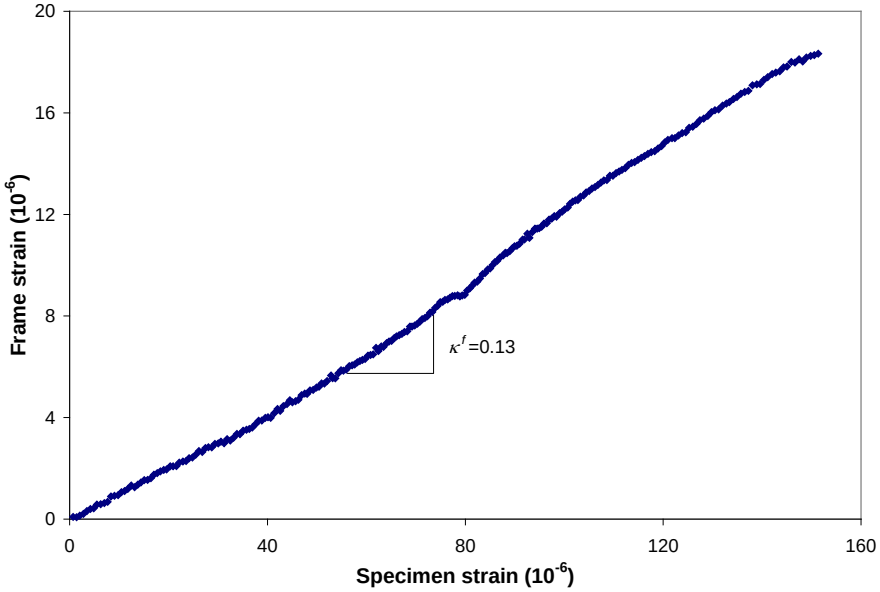

Figure 6. Relationship between frame and specimen strain for "medium" specimen.

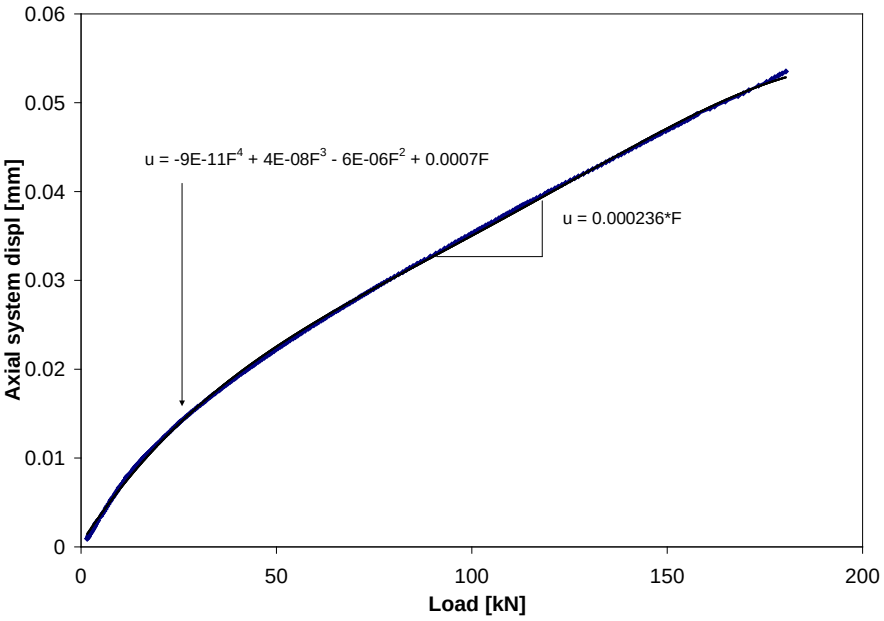

Figure 7. Axial system displacement for "small" biaxial specimen.

The lateral system displacement was linearly related to the load F_1 (Fig. 8). The average lateral compliance $C_L(\sigma_3,A)$ was described with

$$u_3^{sys} = C_L(\sigma_3, A)F_1 \qquad (30b)$$

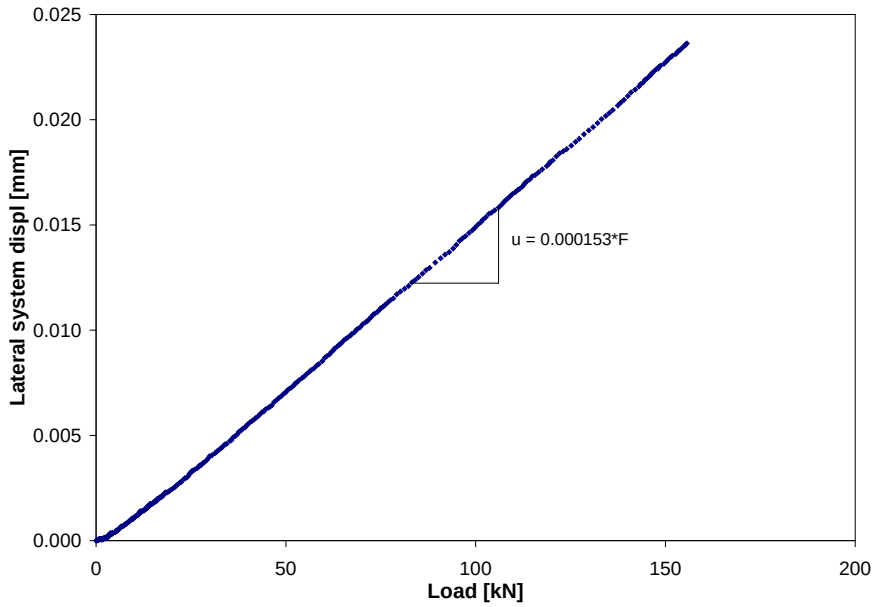

Figure 8. Lateral system displacement for "small" biaxial specimen.

C_A and C_L were calculated to be in the range of 0.23-0.73 micron/kN and 0.14-0.38 micron/kN respectively; they were found to be decreasing with increasing confining pressure, also, they increased with increasing specimen size

Saturation and B-check

After the rock specimen was prepared and placed inside the plane-strain apparatus, a small axial seating load was applied. Then, the specimen was stressed axially and laterally to 3-5 MPa, depending on desired pore pressured to be applied later in the test. Because of the plane-strain condition, hydrostatic loading cannot be achieved. Once the confining pressure was applied, the process of water saturation of the specimen started. Water was pumped from downstream into the specimen with the upstream valve open (Fig. 9). For each step of water injection (5-10 ml/step), the upstream pressure increased to approximately 0.4 MPa and decreased in a minute or so to about 0.2 MPa before the next step of injection. The water started flowing from the upstream valve after injecting about 80 ml, the estimated volume of pore space in the specimen. Further pumping of 50 ml of water through the specimen showed that a mass balance was approximately satisfied.

The technique of back-pressure saturation was used next. The purpose of back pressure is to achieve 100% saturation by forcing any gas into solution of the pore water. Increase of the pore pressure in a partially saturated specimen affects the volume of the gas in the pores in two ways:

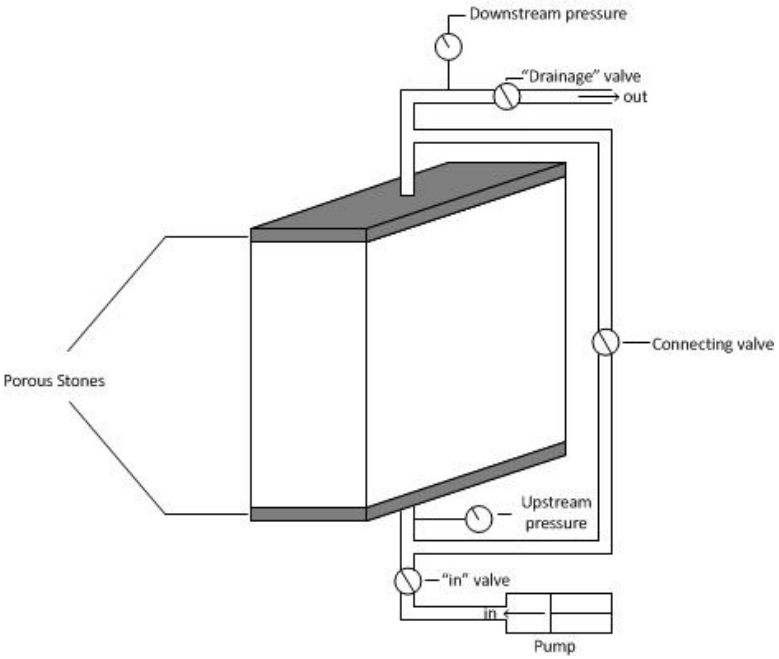

Figure 9. Setup for testing with pore pressure.

(1) by direct compression, the gas is reduced in volume according to Boyle's law; (2) by application of a higher pressure, additional amounts of gas are dissolved in the pore water in accordance with Henry's law of solubility (Lowe and Johnson 1960). Pore pressure u was increased in the specimen by pumping water in and having the drainage valve closed; a maximum back pressure of u = 2-3 MPa was applied. During this procedure, the axial and lateral stresses were always kept 5-6 MPa higher that the pore pressure. After each new increase in back pressure, the pore pressure was allowed to equilibrate, meaning that upstream pressure would be equal to the downstream pressure and the drop of pressure would not exceed 1 kPa/min. During this process the remaining gas was dissolved into the pore fluid. When the equilibration of pressure was achieved, the Skempton's coefficient B was measured; this procedure is called a B-check.

For undrained triaxial tests on soils, Skempton (1954) introduced the pore-pressure coefficient B to express the pore pressure change Δu that occurs due to a change in the all-round pressure $\Delta\sigma$. For soils,

$$B = \frac{\Delta u}{\Delta \sigma} = \frac{1}{1 + \frac{\phi K}{K_f}} \tag{31}$$

and is approximately equal to 1.0, since the bulk modulus of the soil structure (on the order of a few MPa) is negligible with respect to that of the fluid (K_f = 2.2 GPa for water).
Bishop (1973) extended this relation to include the influence of the bulk modulus of the solid material of the skeleton K_s for any porous mass with interconnecting pores. In terms of bulk moduli, it can be written as:

$$B = \frac{\Delta u}{\Delta \sigma} = \frac{1}{1 + \phi\left(\frac{1}{K_f} - \frac{1}{K_s}\right) \Big/ \left(\frac{1}{K} - \frac{1}{K_s}\right)} = \frac{\alpha}{\alpha + \phi K\left(\frac{1}{K_f} - \frac{1}{K_s}\right)} \tag{32}$$

In addition to the interconnectivity of pores, it is assumed that the skeleton and solid material are elastic and isotropic and the pore fluid is linearly compressible. Also, for this case, the change in pressure can be replaced with the change in the mean stress ΔP (Bishop 1973):

$$\Delta P = (\Delta\sigma_1 + \Delta\sigma_2 + \Delta\sigma_3)/3 \tag{33}$$

The increment of the intermediate principal stress can be written as

$$\Delta\sigma_2 = \Delta\varepsilon_2 E + \nu(\Delta\sigma_1 + \Delta\sigma_3) \tag{34}$$

For the tests with pore pressure, the specimen size was chosen in way that when equal increment in axial $\Delta\sigma_1$ and confining $\Delta\sigma_3$ pressures ($\Delta\sigma_1=\Delta\sigma_3=\Delta p$) were applied, the frame deformation due to the stress increment applied by the specimen is compensated by the negative strain on the inner side of the frame due to the increase in cell pressure (according to Lame's solution for a cylinder, the inner part compresses due to equal pressures applied on the inside and outside of the cylinder). So, $\Delta\varepsilon_2=0$ in the equation (34) and the expression for measured B takes form:

$$B^{meas} = \frac{\Delta u}{\Delta P} = \frac{3\Delta u}{2(1+\tilde{\nu})\Delta p} \tag{35}$$

where $\tilde{\nu}$ is current Poisson's ratio of the rock and it changes from ν in dry condition to ν_u upon saturated. When the undrained elastic loading performed on the saturated specimen, ν_u independent of B-values can be calculated from the test data.

While performing an undrained test in the laboratory, the specimen is connected to the drainage system of the cell and also to the pore pressure transducer. As the drainage system has a non-zero volume filled with water, it experiences volume changes due its compressibility. Bishop (1976) modified expression to include terms representing the compressibility of the pore-pressure measuring system. The following equation was obtained for the corrected value of Skempton's coefficient B^{cor}:

$$B^{cor} = \frac{1}{\frac{1}{\left(\frac{\Delta u}{\Delta P}\right)_{observed}} - \frac{V_L}{V}\frac{K}{\alpha K_f} - \frac{K}{\alpha V}\left(C_L + C_M\right)} \tag{36}$$

where V is the volume of the specimen, V_L is the volume of the fluid in the pore-water lines, C_L is the compressibility of the pore-water lines, and C_M is the compressibility of the pore-pressure measuring element. However, several researchers (Bishop 1976; Mesri *et al.* 1976; Ghabezloo and Sulem 2009) noticed that for modern high-pressure tubes and pressure transducers, the main contribution (more than 90%) to the correction term comes from the extra fluid volume in the system V_L. So, only the first two terms in the denominator of the right hand side of (36) are considered. The final equation for calculating B^{cor}, which should be used while solving the system of poroelastic equations (34), becomes

$$B^{cor} = \frac{1}{\left(\frac{2(1+\nu_u)\Delta p}{3\Delta u}\right) - \frac{V_L}{V}\frac{K}{\alpha K_f}} \tag{37}$$

The parameters measured in two drained tests (BxBS-6d and BxBS-11d) and in three undrained tests (BxBS-2u, BxBS-3u, and BxBS-12u) are presented in Table 1.

Table 1. Results of two drained tests (BxBS-6d and BxBS-11d) and three undrained tests (BxBS-2u, BxBS-3u, and BxBS-12u).

Test #	P [MPa]	u [MPa]	E [GPa]	ν	K, K_u [GPa]	G [GPa]
BxBS-6d	6	0	10.9	0.31	9.6	4.2
BxBS-11d	5	0	10.8	0.32	10.0	4.1
BxBS-2u	8	2.6	13.2	0.34	13.8	4.9
BxBS-3u	10	3.8	13.5	0.35	15.0	5.0
BxBS-12u	10	3.4	15.3	0.34	15.9	5.9

Acoustic emission

Failure of rock involves microcracking, which generates elastic waves known as acoustic emission (AE). The AE system used in the plane strain tests consisted of eight sensors at known positions, four on each side of the prismatic specimen subjected to confining pressure. By recording the time histories and identifying the arrival time of the P-wave, it is possible to locate the event with an error of a few mm. The AE signals were recorded by a computer automated measurement and control data acquisition system, equipped with four DAQ cards (National Instruments model PCI-5112). Each card has two individual 8-bit analog to digital converters, and a sampling rate of 20 MHz was set to record AE signals that are conditioned by bandpass filters from 0.1 – 1.2 MHz and 40dB gain. The transducers have a diameter of approximately 3 mm, with the frequency response from 0.1 – 1 MHz. All channels were triggered when the signal amplitude exceeded a threshold on the anchor sensor. A program coded with LabView controls the signal acquisition over a 200 μs window, with a 100 μs pretrigger.

A common type of source location algorithm involves the arrival time of the P-wave. Microseismic activity due to a change in stress or environment is recorded by each sensor with a known position at a given time. From the relative arrival times of the P-wave and the measured P-wave velocity of the material, the event hypocenter can be estimated with a minimum of five sensors. The problem contains four unknowns: the spatial coordinates x, y, z of the event and the time at which the event occurred, but a fifth sensor (or other information) is needed to remove ambiguities arising from the quadratic nature of the distance equation. Because some error is associated with arrival-time detection (it is not always clear when a low amplitude signal arrives) and with the P-wave velocity (as damage accumulates material properties may change or become anisotropic), the number of sensors should be increased so that the location problem becomes over-determined. Then a solution scheme can be developed whereby the error is minimized to obtain a best-fit type of solution, and statistical methods can be used to evaluate the fit.

The distance r_i between the source and the ith sensor is related to the P-wave velocity c_p by

$$r_i = c_p\left(t_i - t\right) + \varepsilon_i \tag{38}$$

where t = time at which the event occurs, t_i = arrival time at the ith sensor, and ε_i = residual of computed distances. From (38), it can be seen that a time shift does not affect the source location, so an arbitrary time base can be selected. The travel distance r_i can be expressed by the unknown source coordinates (x, y, z) and the known sensor coordinates (x_i, y_i, z_i) by

$$r_i = \sqrt{(x_i - x)^2 + (y_i - y)^2 + (z_i - z)^2} \tag{39}$$

The sum of the squares of the residuals ε_i can be written

$$I = \sum_{i=1}^{N} \varepsilon_i^2 \tag{40}$$

where N = the number of sensors. The unknowns x, y, z and t can be determined using a least-squares method by minimizing I. However, the equations are nonlinear in the source coordinates x, y, z, so the minimization is carried out numerically using the Levenberg-Marquardt algorithm. The first estimate of x, y, z is obtained by a linearization of the equations (40).

Acoustic emission locations were determined for specimens BxBS-6d and BxBS-7. For more accurate determination of AE locations, P-wave velocity was measured at different effective stresses. For the tests described, c_p at 5 MPa effective pressure was found to be 2700 m/s, compared to 2100 m/s for a dry specimens at atmospheric pressure. Processing of the AE data recorded for BxBS-7 test provided 1834 locations with error less than 3 mm, out of 9254 total events. Before the peak load was reached, AE events were scattered in the specimen (Fig. 10a). However, in the post peak response, located events closely follow the failure mechanism (Fig. 10b and 10c).

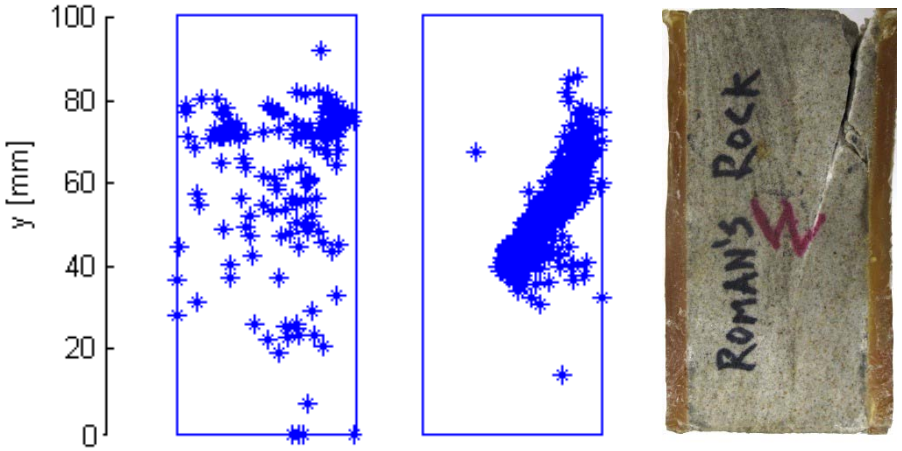

Figure 10. Fracture and the location of AE events for BxBS-7 specimen.

The significant difference between drained and undrained compression in terms of the change of AE rate with loading was observed. For the test where the pore pressure inside the rock was constant, the number of AE events per load step remarkably increased when the axial load on the specimen reached approximately 70% of peak load (Fig. 11), which is also the case for air-dry experiments. However, in an undrained test, only a few microseismic events were recorded prior

to failure of the specimen (Fig. 12). The abrupt change in the slope of AE rate curve happens only when the pore pressure in the rock drops significantly due to localization of deformation and appearance of a macrocrack. This effect could be explained by the delayed tendency to dilate for the rock under an undrained condition and the fact that an increase in specimen volume is usually accompanied by the intense microcracking, hence the AE rate should be increasing.

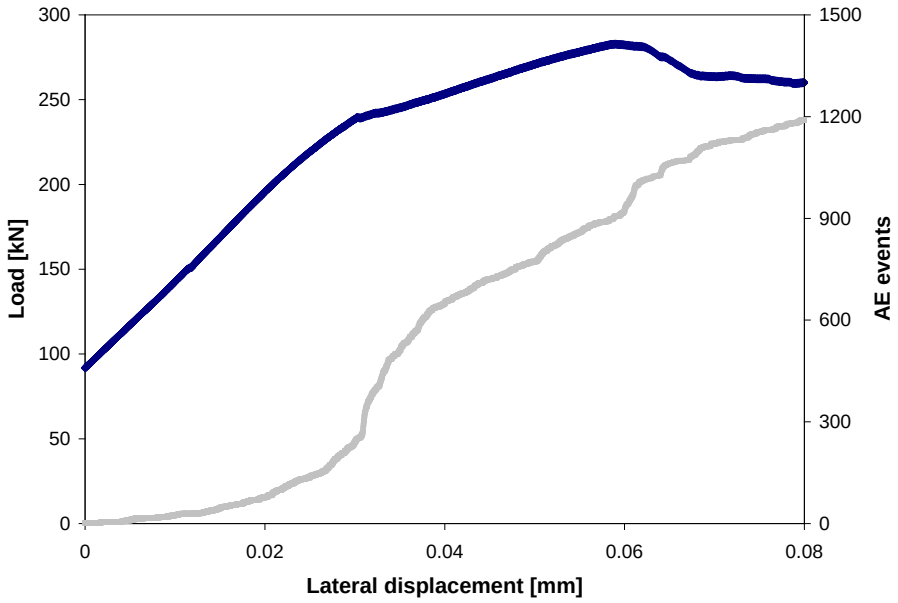

Figure 11. AE data for drained plane strain test.

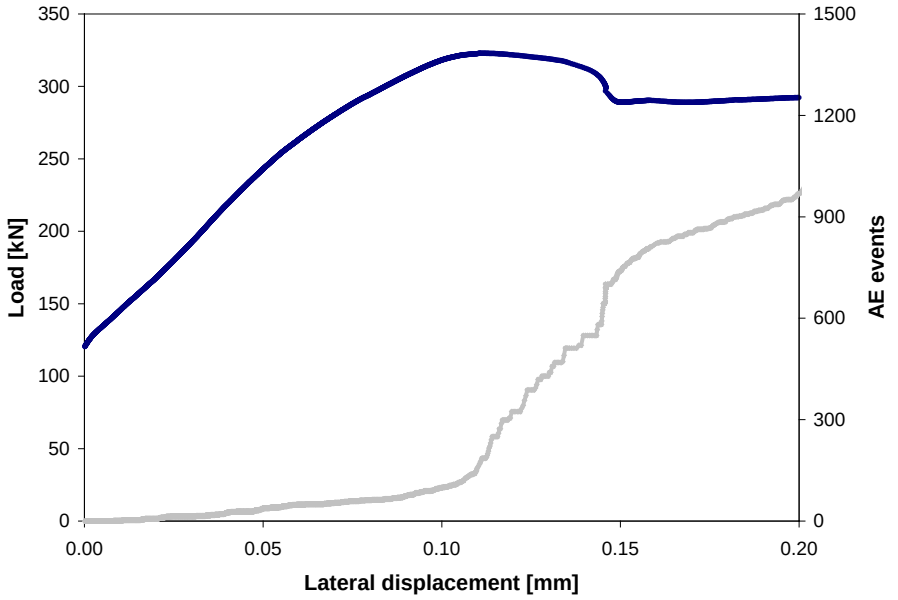

Figure 12. AE data for undrained plane strain test.

RESULTS AND DISCUSSION

Performing experiments with the UMN plane strain apparatus, we are limited in the magnitude of maximum principal stress (< 115 MPa) and effective confinement (< 10 MPa) that we can apply to fail the specimen of a particular size. Also, under these conditions, the failure planes are still quite tortuous, so the fracture inclination angle varies along the specimen height.

The constitutive model chosen for describing the inelastic response of brittle rock, including the effects of the pore fluid, was formulated by Rice (1975) for the special deformation state of confined shearing. It illustrates the hardening effect of dilatancy-induced pore pressure reductions. The model was reformulated by Rudnicki (1985) in terms of poroelastic parameters (Rice and Cleary 1976) for rock subjected to pore pressure p, shear stress τ, and hydrostatic (mean) stress σ.

For a stress increment $d\tau$, $d(\sigma–p)$ that involves continued inelastic deformation, the increment of total shear strain $d\gamma$ is

$$d\gamma = d\tau/G + d^{p}\gamma \tag{41}$$

where $d^{p}\gamma$ is the inelastic (plastic) increment of shear strain. An increase in hydrostatic compression inhibits inelastic deformation in brittle rock. Thus, the inelastic increment of shear strain takes the following form:

$$d^{p}\gamma = \left(d\tau - \mu d(\sigma - p)\right)/H \tag{42}$$

where H is an inelastic hardening modulus (Fig. 13a) and μ is a friction parameter. It represents the effect of effective normal stress in inhibiting failure and can be measured as the local slope of the yield surface (separating elastic and inelastic states) in the plane of τ and $(\sigma–p)$, as shown in Fig. 13b.

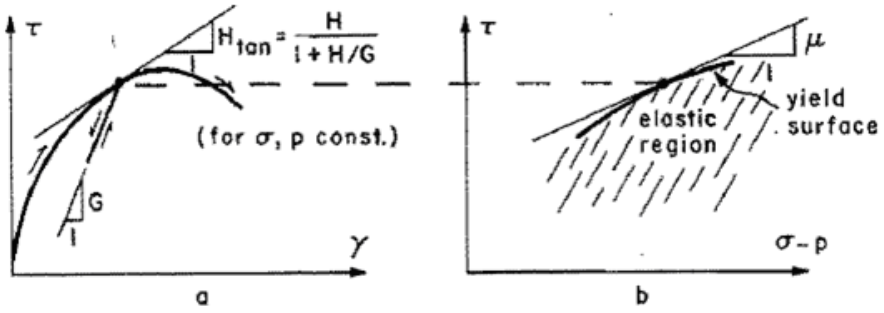

Figure 13. Stress-strain data for saturated rock (Rice 1975). (a) Shear stress-strain relation under drained conditions, σ and p being constant. (b) Effect of effective compressive stress on shear stress required for continuing inelastic deformation.

For the case when there is no change in pore pressure during the deformation (dp = 0 or drained response) and the hydrostatic stress is constant, $d\gamma$ can be written as

$$d\gamma = \frac{d\tau}{G} + \frac{d\tau}{H} \tag{43}$$

The inelastic volume strain arises from processes that accompany inelastic shear and its increment is assumed to be given by β, the dilatancy factor ($\beta < 0$ for compaction). For applications to rock, it is assumed that μ, β, and G are constant over some range of loading.

For dilatant inelastic deformation ($\beta > 0$) under undrained condition, the pore fluid pressure p tends to decrease and the following expression was obtained (Rudnicki 1985) for the increment of shear strain ($d\sigma = 0$ for convenience):

$$d\gamma = d\tau/G + d\tau/\left(H + \mu\beta K_{eff}\right) \tag{44}$$

where K_{eff} can be written as follows:

$$1/K_{eff} = \left(\phi + \Delta\phi\right)\left(1/K_f - 1/K_s''\right) + \alpha/K \tag{45}$$

The expression obtained for $\Delta\phi$ (change of porosity in the stressed state) by Detournay and Cheng (1993) is

$$\Delta\phi = -\left(\alpha - \phi\right)\left(\sigma - u\right)/K - \phi\left(1/K_s' - 1/K_s''\right)p \tag{46}$$

The hardening modulus in equation (44) has been augmented by the term $\mu\beta K_{eff} > 0$, hence the response is stiffer and the rock is said to be dilatantly hardened (Fig. 14).

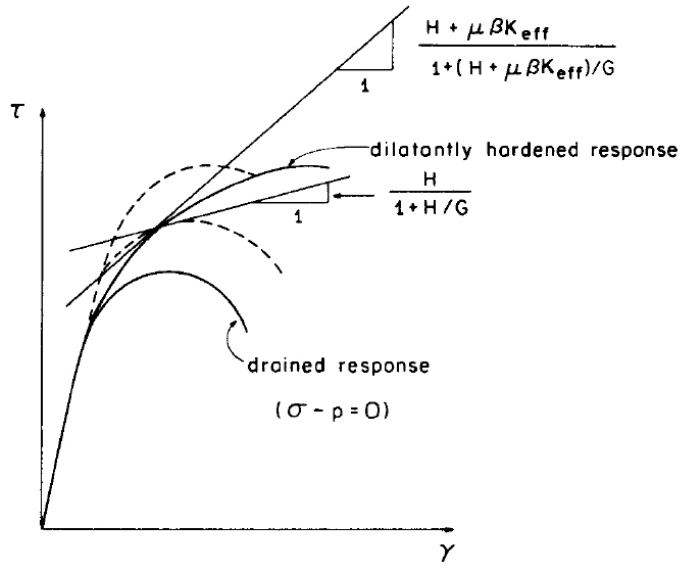

Figure 14. Dilatant hardening due to undrained conditions (Rudnicki 1985).

Experimental observations

In the Rice-Rudnicki model, dilatant hardening is described for the condition of constant mean stress. This condition is not usually preserved in tests, where the prismatic specimens are loaded axially at constant confining pressure σ_3. For example, volumetric strain $\varepsilon = \varepsilon_1 + \varepsilon_3$ is plotted as a function of shear stress $\gamma = \varepsilon_1 - \varepsilon_3$ for drained and undrained tests (Fig. 15 and 16). Because of the initial stress state for both experiments, the specimens compact (the sign convention is compression positive) before they dilate. It can also be seen that in the undrained test, Fig. 16,

pore pressure is increasing from 2.8 to 7.2 MPa when the sandstone is compacting, and it starts decreasing only when the deformation of the specimen becomes inelastic (volumetric strain response deviates from linearity).

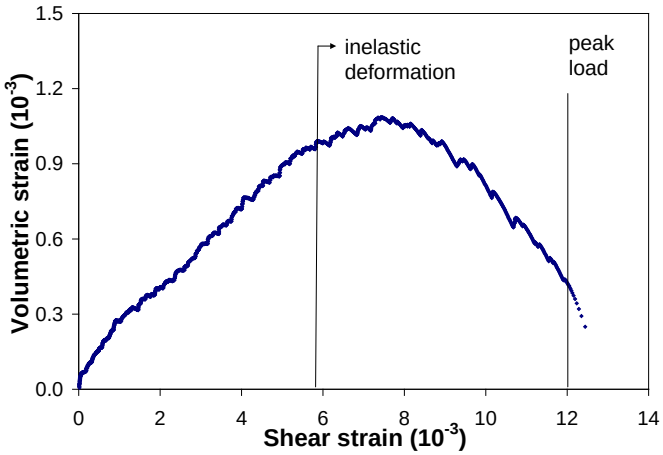

Figure 15. Volumetric strain for the drained test (BxBS-4d).

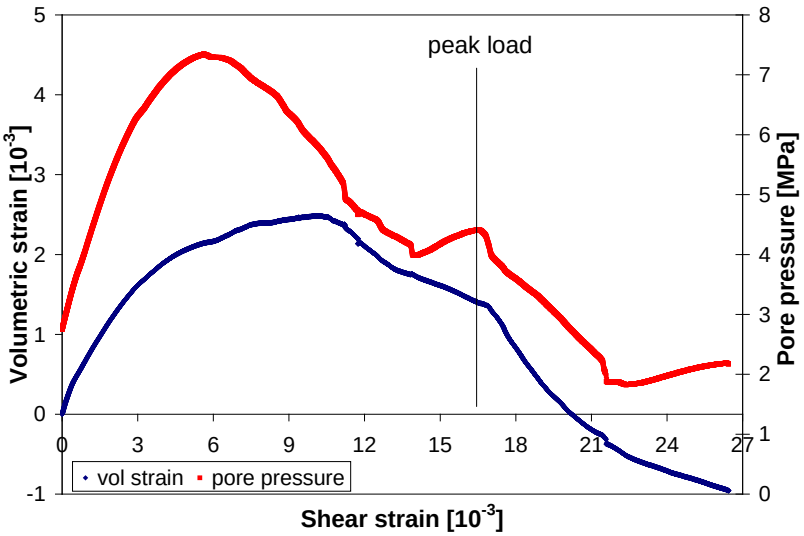

Figure 16. Volumetric strain (dark blue) and pore pressure (red) for the undrained test (BxBS-12u).

Because of the significant amount of compaction experienced by the rock prior to dilatancy, other conditions need to be implemented into the constitutive model. We will compare a pair of drained and undrained experiments conducted where the effective (Terzaghi) mean stress is the same when the response of the rock becomes inelastic. As an example, two plane strain experiments are compared: BxBS-4d – drained test, which was performed with σ_3 = 5.1 MPa and initial pore pressure p = 0.6 MPa, and BxBS-12u – undrained test with σ_3 = 10.0 MPa and initial pore pressure p = 2.8 MPa (Fig. 16). Plane strain deformation allows us to consider plane shear stress $\tau = (\sigma_1 - \sigma_3)/2$ and plane mean stress $s = (\sigma_1 + \sigma_3)/2$, and effective mean stress $s' = s - p$ for the drained and undrained tests (Fig. 17 and 18). Note that the collection of the data in the drained test has started from a non-zero shear stress.

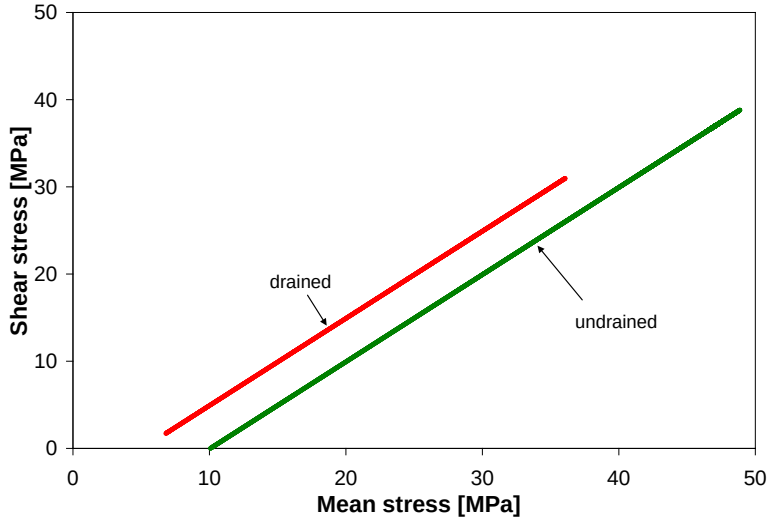

Figure 17. Shear stress - mean stress for drained and undrained tests (BxBS-4d and BxBS-12u).

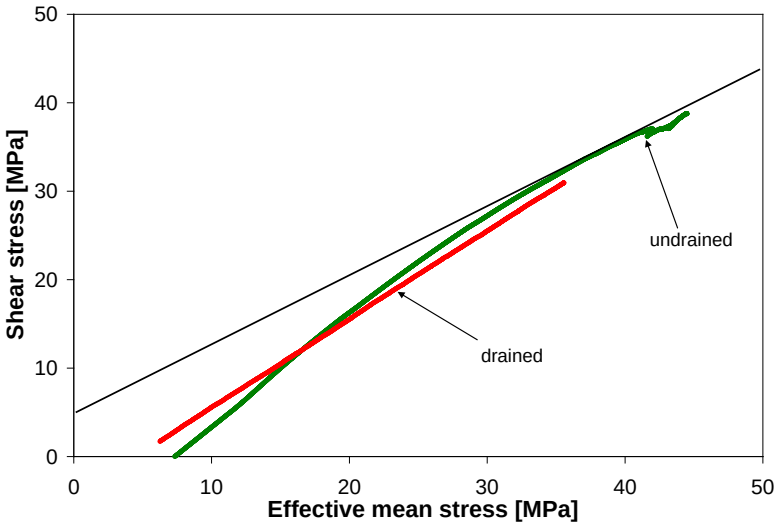

Figure 18. Shear stress - effective mean stress for drained and undrained tests (BxBS-4d and BxBS-12u).

It can be seen that even though the mean stresses are different for these two tests, the effective mean stresses behave similarly (Fig. 18), which makes their comparison in terms of dilatant hardening appropriate. The effective mean stress at the beginning of undrained shearing is slightly larger than that in the drained test (for the same level of shear stress). However for $\tau =$ 12 MPa, drained and undrained effective stresses become equal and then further in loading the latter one becomes slightly smaller than the corresponding effective stress for the drained test. It happens because pore pressure increases at the initial stage of undrained shearing, and then decreases because of the dilatancy, but the pore pressure is still larger at the peak load than its initial value (Fig. 16).

Shear stress - shear strain response for BxBS-4d and BxBS-12u is presented in Fig. 19. It can be seen that the undrained response is stronger, as predicted by the Rice-Rudnicki model, starting from a value of $\gamma = 2.2\times10^{-3}$.

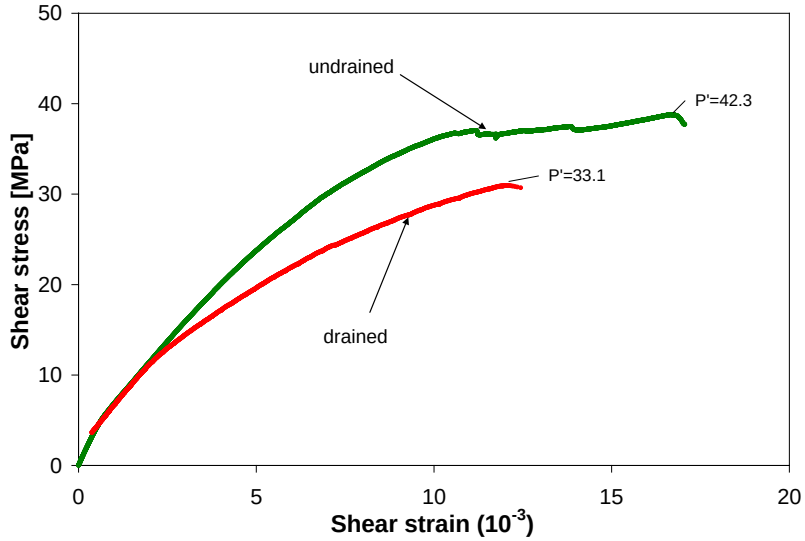

Figure 19. Shear stress - shear strain for drained and undrained tests (BxBS-4d and BxBS-12u).

Measurements of hardening parameters

The measured principal strains contain both the elastic and plastic components. The onset of the nonlinear response was used as a benchmark signifying when plastic deformation initiated (Fig. 15). The plastic strains were determined by removing the calculated elastic response from the measured deformation assuming no change in elastic parameters (Riedel and Labuz 2007):

$$d\varepsilon^p = d\varepsilon^{meas} - d\varepsilon^e \tag{47}$$

$$d\gamma^p = d\gamma^{meas} - d\gamma^e \tag{48}$$

For the drained test (BxBS-4d) conducted at 4.5 MPa effective confinement, plastic deformation was only associated with a dilatant response (Fig. 20). The increase of plastic volumetric strain was fairly linear from the onset of inelasticity up to the peak. The dilatancy angle ψ is defined by

$$\sin\psi = -\frac{d\varepsilon^p}{d\gamma^p} \tag{49}$$

Dilatancy angle calculated for the drained test is presented in Fig. 21. It can be seen that even though the data are scattered, for $\gamma^p > 0.5\times10^{-3}$ the dilatancy angle of the sandstone becomes approximately constant and equal to 24°. Hence, the dilatancy factor β

$$\beta = \sin\psi \tag{50}$$

is taken as a constant value $\beta = \sin 24° \approx 0.41$.

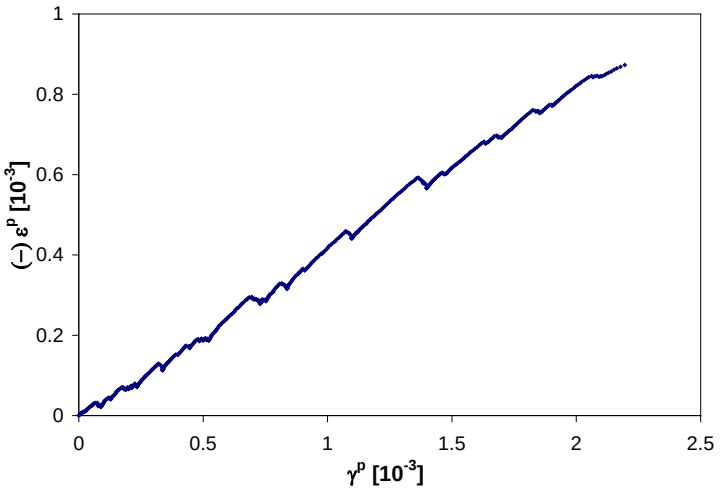

Figure 20. Dilatancy behavior for the drained test (BxBS-4d).

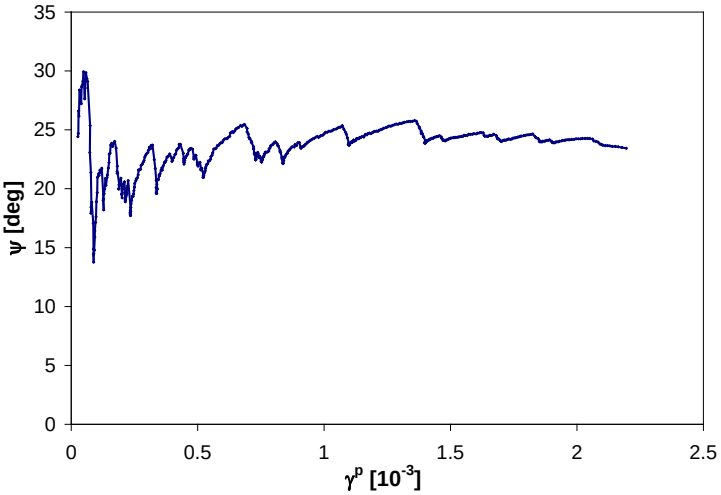

Figure 21. Development of dilatancy angle after the onset of inelastic deformation (BxBS-4d).

For in-plane shear stress τ and mean stress s, the Mohr-Coulomb linear yield function can be written as (Riedel and Labuz 2007)

$$\xi = \frac{\tau}{s - Q} \tag{51}$$

$$\xi = \sin(\varphi) \tag{52}$$

and φ is the friction angle. The parameter Q is the intercept at $\tau = 0$; for the tested Berea sandstone with the linear failure envelope, Q = -3.8 MPa (Fig. 22).

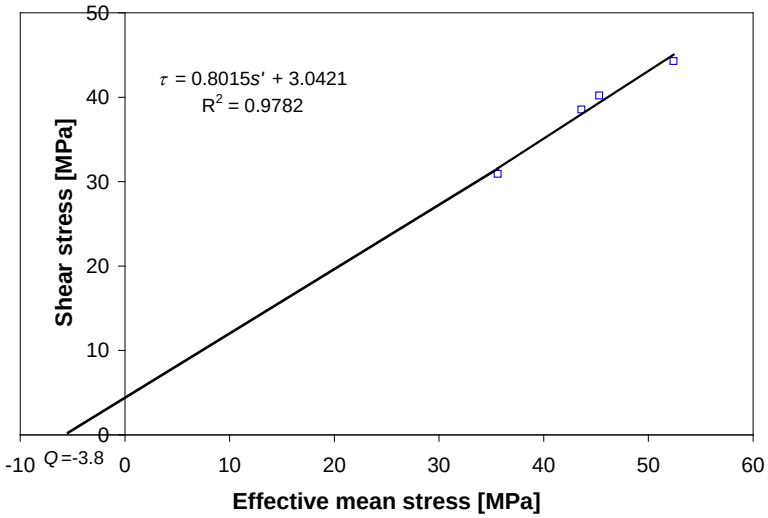

Figure 22. Failure envelope for drained Berea sandstone in τ-s plane.

Friction coefficient μ, which is used in the dilatant hardening model, can be written as

$$\mu = \tan\varphi \tag{53}$$

We are interested in behavior of μ only for inelastic deformation. Calculating μ from ξ, we can present it as a function of plastic shear strain γ^p (Fig. 23). It appears that the friction coefficient μ is approximately constant throughout the inelastic deformation process, and it is taken as μ = 1.2 in the calculation of dilatantly hardened response.

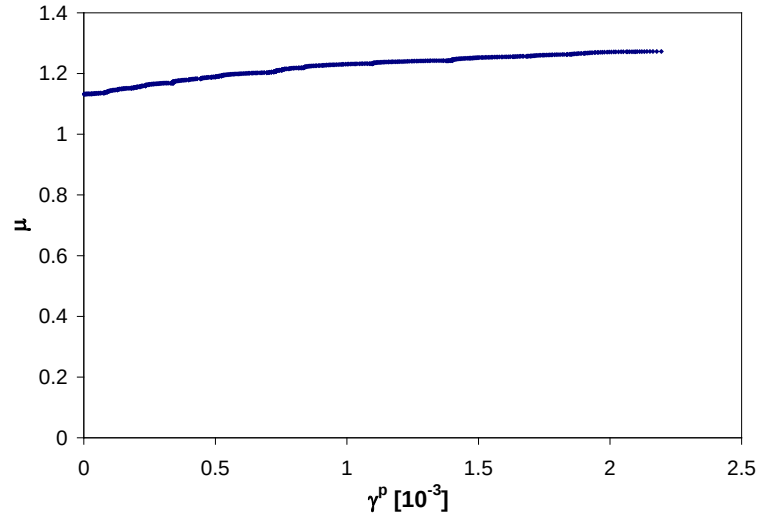

Figure 23. Friction parameter μ for the drained test (BxBS-4d).

K_{eff} is the parameter that links the poroelastic response of the material with the dilatant hardening model. To be able to calculate K_{eff}, the change in the porosity $\Delta\phi$ during deformation needs to be estimated. From equation (46), it can be seen that $\Delta\phi$ has "stress" in the numerator with order of MPa, and poroelastic bulk modulus in the denominator with order of GPa. Hence $\Delta\phi \sim 0.01$ and

is on the order of the accuracy of our porosity measurements, so it can be neglected. The poroelastic parameters measured and calculated from drained and undrained experiments (Makhnenko and Labuz 2012) are the following:

$$\phi = 0.23, \quad \alpha = 0.66, \quad K = 10 \ GPa, \quad K_s" = 5.7 \ GPa \tag{54}$$

The bulk modulus of the fluid can be taken as that of pure water (K_f = 2.24 GPa), because we assume that the specimen is fully saturated prior to shear loading (Makhnenko and Labuz 2013). Substituting the values, we obtain

$$K_{eff} = 7.8 \ GPa \tag{55}$$

Shear modulus of Berea sandstone is calculated from the initial part of loading in Fig. 19:

$$G = \frac{d\tau}{d\gamma^e} = 4.6 \ GPa \tag{56}$$

The inelastic hardening modulus H can be calculated for each new increase of shear strain γ due to increasing shear stress τ:

$$H = \frac{1}{\frac{d\gamma}{d\tau} - \frac{1}{G}} \tag{57}$$

The data were recorded every one second, which means that H can be calculated for each

$$\Delta\gamma = 0.007\times10^{-3} \tag{58}$$

increment of shear strain (the shear strain rate was approximately constant during the test). To describe the corresponding undrained response, increments of shear stress are

$$\frac{d\tau}{d\gamma} = \frac{H + \mu\beta K_{eff}}{1 + \left(H + \mu\beta K_{eff}\right)/G} \tag{59}$$

Substituting the previously calculated values of G, μ, β, K_{eff} (constants), the undrained response predicted by dilatant hardening model can be obtained from the corresponding drained data. The results of the drained and undrained tests (BxBS-4d and BxBS-12u, respectively), along with the model prediction, are presented in Fig. 24.

The response predicted by the model is slightly stiffer than the experimental undrained response at the beginning of loading ($\gamma < 3.8\times10^{-3}$). At higher shear stresses, the model predicts undrained behavior fairly well almost up to the point when the specimen starts to fracture. In the last region of undrained inelastic deformation, increase of axial stress "tries" to facilitate failure but the increase of the effective confinement due to dilatancy delays it. The presence of these two competing factors explains why it takes about the half of the total shear strain ($\Delta\gamma \sim 8\times10^{-3}$) to bring the specimen from 90% of the peak stress to failure.

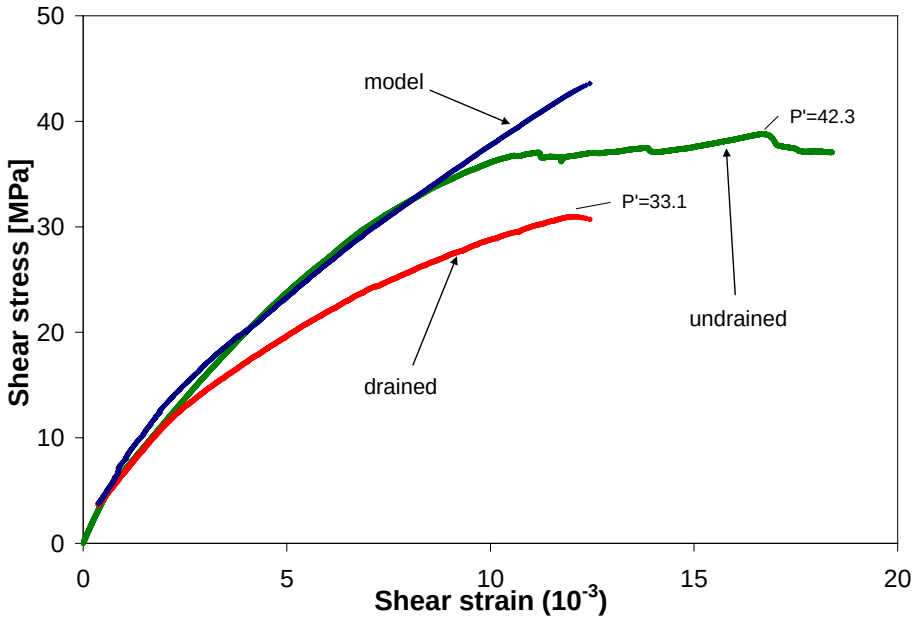

Figure 24. Results of drained and undrained tests (BxBS-4d and BxBS-12u) and dilatant hardening model.

Similar behavior is observed for another pair of drained (BxBS-11d) and undrained (BxBS-8u) experiments (Fig. 25). The drained test was conducted at 5.5 MPa confinement and 0.1 MPa pore pressure, while the undrained test had σ_3 = 8 MPa and started from 1.6 MPa pore pressure. Here, the dilatant hardening model closely predicts the undrained inelastic behavior almost up to the peak load.

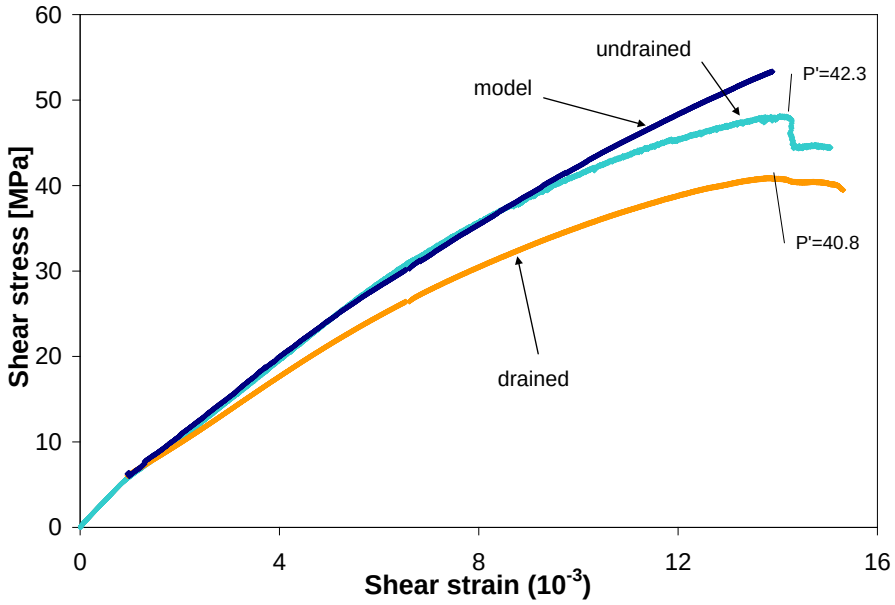

Figure 25. Shear stress - shear strain for drained and undrained tests (BxBS-11d and BxBS-8u).

NUMERICAL METHOD

Consider a finite or an infinite isotropic elastic domain characterized by the shear modulus and the Poisson's ratio and containing fractures of arbitrary shapes (Fig. 26 a,b). The load in the domain may be applied either locally (in the form of point forces), or via the boundaries of the domain including those of the fractures (in the form of boundary tractions). In case of an infinite domain, the load may be also applied via the far field stress. In addition, the medium could be subject to constant body forces (*e.g.* gravity). The load at the fractures' surfaces could be due to various physicals effects e.g. fluid pressure. The elastic fields inside of the domain are to be defined.

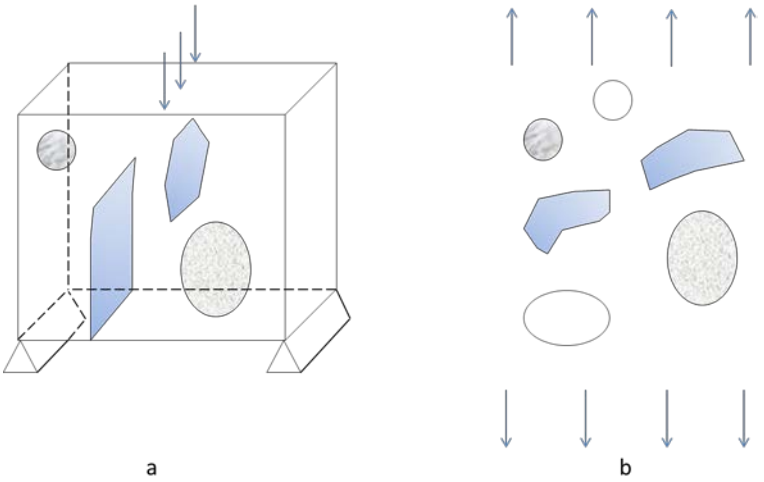

Figure 26. Problem formulation. Finite and infinite computational domain.

In the present work, the boundaries are approximated by a set of planar triangular elements. The piecewise constant approximations of the boundary unknowns are employed. Approximations of higher order will be used in future work. For each boundary element, a local Cartesian coordinate system is introduced. The boundary unknowns are defined from the system of algebraic equations set up to satisfy the boundary conditions at the defined set of points (collocation points). Due to the use of constant approximations, the centers of the triangles are the natural choice for the collocation points. The details are contained in the Appendix.

The approach has been tested on a number of analytical and numerical benchmark problems:

- the problem of a single penny-shaped crack in infinite medium subject to either normal or shear far-field stress,
- the plane strain problem of a half-circular crack in the infinite domain with biaxial far-field load.

The latter problem can be simulated by considering a three-dimensional crack shaped as a long half-cylinder with dimension in the axial direction much larger as compared to the other directions and loaded perpendicularly to its axis. The results for the benchmark problems as well as the comments on the reference solutions are given in the Appendix.

CONCLUSION

Deformation and damage of a porous, fluid-saturated rock under drained and undrained conditions were investigated. A plane-strain apparatus was modified in order to conduct tests with water-saturated rock specimens and to measure the pore pressure within the rock. Transducers within the apparatus were calibrated at the various loading states and the compliances of the system were determined. Plane strain compression and conventional triaxial compression tests were performed at different confining pressures under air-dry, drained, and undrained conditions. The behavior of the rock was evaluated within the framework of linear poroelasticity. Dilatant hardening and contractant softening was investigated from undrained experiments, where pore pressure was measured throughout the failure process. The parameters that govern the inelastic deformation of fluid-saturated rock, *i.e.* dilatancy angle β, friction coefficient μ, poroelastic coefficient K_{eff}, shear modulus G, and inelastic hardening modulus H, were calculated for the drained response. The constitutive model predicts the undrained inelastic response of the rock fairly well, almost up to the peak load if compared with the undrained test that had the same effective mean stress at the onset of inelasticity. Knowledge of dilatant hardening behavior is essential for the proper assessment of underground structures, such as long-term CO_2 storage facilities.

REFERENCES

Aldrich, M.J. 1969. Pore pressure effects on Berea sandstone subjected to experimental deformation. *Geol. Soc. Am. Bull.* 80:1577-1586.

Berge, P. A. 1998. Pore compressibility in rocks. *Poromechanics: A Tribute to Maurice A. Biot, Proceedings of the Biot Conference on Poromechanics, Louvain-la Neuve, Belgium,* 351-356.

Biot, M.A. 1941. General theory of three-dimensional consolidation. *J. Appl. Phys.,* 12: 155-164.

Biot, M.A., D.G. Willis. 1957. The elastic coefficients of the theory of consolidation. *J. Appl. Mech.,* 594-601.

Biot, M.A. 1973. Nonlinear and semilinear rheology of porous solids. *J. Geophys. Res.,* 78:4924-4937.

Bishop, A. W. 1973. The influence of an undrained change in stress on the pore-pressure in porous media of low compressibility. *Geotechnique,* 23(3): 435–442.

Bishop, A. W. 1976. Influence of system compressibility on observed pore pressure response to an undrained change in stress in saturated rock. *Géotechnique,* 26(2):371-375.

Brace, W.F. and R.J. Martin. 1968. A test of the law of effective stress for crystalline rocks of low porosity. *Int. J. Rock Mech. & Mining Sci*., 5:415-436.

Brown, R. J. and J. Korringa. 1975. On the dependence of the elastic properties of a porous rock on the compressibility of the pore fluid: *Geophysics,* 40:608–616.

Detournay, E., A. Cheng. 1993. Fundamentals of poroelasticity. In *Comprehensive Rock Engineering, Vol. II,* ed. C. Fairhurst, 113-171.

Dehler, W. and J.F. Labuz. 2007. Stress path testing of anisotropic sandstone. *J. Geotech. Geoenviron. Eng.*, 133:116-119.

Fatt, I. 1959. The Biot-Willis coefficients for a sandstone. *J. Appl. Mech.* 26:296-297.

Frank, F.C. 1965. On dilatancy in relation to seismic sources. *Reviews of Geophysics*, 3 (4): 485-503.

Gassman, F. 1951. Über die elastizität poröser medien. *Vierteljahrsschriftder Naturforschenden Gessellschaft in Zurich*, 96:l–23.

Gassman, F. 2007. On elasticity of porous media (translation of the 1951 paper from the German). In *Classics of elastic wave theory: SEG*, eds. M. A. Pelissier, H. Hoeber, N. van de Coevering, and I. F. Jones, 389–407.

Geertsma, J. 1957. The effect of fluid pressure decline on volumetric changes of porous rocks. *Soc. Petr. Eng.*, 210:331-340.

Ghabezloo, S. and J. Sulem. 2009. Effect of the volume of the drainage system on the measurement of undrained thermo-poro-elastic parameters. *Int. J. Rock Mech. & Mining Sci*., 47:60-68.

Green, D.H. and H.F. Wang. 1986. Fluid pressure response to undrained compression in saturated sedimentary rock, *Geophysics*, 51:948–956.

Hart, D.J. and H.F. Wang. 1995. Laboratory measurements of a complete set of poroelastic moduli for Berea sandstone and Indiana limestone. *J. Geophys. Res.*, 100:17,741–17,751.

Hart, D.J. and H.F. Wang. 2010. Variation of unjacketed pore compressibility using Gassmann's equation and an overdetermined set of volumetric poroelastic measurements. *Geophysics*, 75:9-18.

Labuz, J.F., S.-T. Dai, and E. Papamichos. 1996. Plane-strain compression of rock-like materials. *Int. J. Rock Mech. Min. Sci.*, 33(6): 573-584.

Lei, X., T. Tamagawa, K. Tezuka, and M. Takahashi. 2011. Role of drainage conditions in deformation and fracture of porous rocks under triaxial compression in the laboratory. *Geophys. Res. Letters*, 38, L2430.

Lin, Q., J.F. Labuz, and S. Cattaneo. 2010. Digital Image Correlation and the Fracture Process in Rock. In *Proceedings of 44th US Rock Mechanics Symposium and 5th U.S.-Canada Rock Mechanics Symposium, Salt Lake City, 27-30 June 2010.*

Lockner, D.A and S.A. Stanchits. 2002. Undrained poroelastic response of sandstones to deviatoric stress change. *J. Geophys. Res.*, 107:2353-2366.

Lowe, J. and T.C. Johnson. 1960. Use of back pressure to increase degree of saturation of triaxial test specimen. In *Conference on Shear Strength of Cohesive Soils*, 819-836.

Makhnenko, R.Y., J.J. Riedel, and J.F. Labuz. 2011. Undrained plane strain compression of shale. In *Proceedings of 45th US Rock Mechanics/Geomechanics Symposium, San Francisco, 26-29 June 2011.*

Makhnenko, R., and J. Labuz. 2012. Drained and Undrained Plane Strain Compression of Porous Rock. In *Proceedings of XXIII ICTAM, Beijing, China, 19-24 August 2012*, paper No. FS10-020

Makhnenko, R.Y., and J.F. Labuz. 2013. Saturation of the porous rock and measurement of the *B*-coefficient. Submitted for *the 46th U.S. Rock Mechanics/ Geomechanics Symposium, San Francisco, 23-26 June 2013*, paper No. 468.

Mesri, G. K., K. Adachi, and C.R. Ullrich. 1976. Pore-pressure response in rock to undrained change in all-round stress. *Geotechnique*, 26(2):317–330.

Nur, A. 1972. Dilatancy, pore fluids, and premonitory variations of t_s/t_p travel times. *Bull. Seismol. Soc. Amer.*, 62:1217-1222.

Nur, A. and J.D. Byerlee. 1971. An exact effective stress law for elastic deformation of rock with fluids. *J. Geoph. Res*., 76:6414–6419.

Rice, J.R. 1975. On the stability of dilatant hardening for saturated rock masses. *J. Geophys. Res.*, 80(11): 1531-1536.

Rice, J. R. 1977. Pore pressure effects in inelastic constitutive formulations for fissured rock masses. In *Advances in Civil Eng. through Eng. Mech., ASCE*, 360-363.

Rice, J.R., and Cleary, M.P. 1976. Some basic stress diffusion solutions for fluid-saturated elastic porous media with compressible constituents. *Rev. Geophys. and Space Phys.*, 14: 227-241.

Rice, J.R. and J.W.Rudnicky. 1979. Earthquake precursory effects due to pore fluid stabilization of a weakening fault zone. *J. Geophys. Res.*, 84:2177-2194.

Riedel, J.J. and J.F. Labuz. 2007. Propagation of shear band in sandstone. *Int. J. Numer. Anal. Meth. Geomech.*, 31:1281-1299

Rudnicki, J.W. 1985. Effect of pore fluid diffusion on deformation and failure of rock. In *Mechanics of Geomaterials*, ed. Z. P. Bažant, New York: John Wiley & Sons, 315-347.

Scholz, C.H., L.R. Sykes, and Y.P. Aggarwal. 1973. Earthquake prediction: a physical basis. *Science*, 181:803-810.

Skempton, A.W. 1954. The pore-pressure coefficients A and B. *Geotechnique*, 4:143-147.

Sulem, J. and H. Ouffroukh. 2006. Hydromechanical behavior of Fontainebleau sandstone. *Rock Mech. Rock Engng*., 39(3):185-213.

Terzaghi, K. 1936. The shearing resistance of saturated soils and the angle between the planes of shear. In *Proceedings of International Conference on Soil Mechanics and Foundation Engineering.* Harvard University Press, Cambridge, Mass., 1;54-56

Vardoulakis, I. 1996. Deformation of water-saturated sand: I. uniform undrained deformation and shear banding. *Geotechnique*, 46(3):441-456.

Vardoulakis, I. 1996. Deformation of water-saturated sand: II. The effect of pore water flow and shear banding. *Geotechnique*, 46(3):457-471.

APPENDIX

1 Introduction

Understanding the mechanisms of rock fracture is of key importance to the mining and petroleum industries. Rock masses feature complicated geometry and structure including joints, heterogeneities of different scales (e.g. grains, pores, macroscopic inhomogeneities, etc.) and may be subject to various effects (e.g. fluid pressure, temperature gradient, etc.). Although many aspects of rock behavior have been extensively studied, there is still a strong demand for comprehensive computational models that would allow to accurately treat complex behavior of rock masses. Among the numerical methods used for geomechanical modelling, the Boundary Element Method (BEM) deserves special attention due to its capability of efficient treatment of problems that include large (infinite) heterogeneous domains containing fractures of arbitrary shapes. It allows for accurate resolution of extreme stress gradients inherent to the fracture front (crack tip). While two-dimensional Boundary Element computational models are widely available, comprehensive three-dimensional models are still lacking.

2 Objectives of research

The objective of this research is to develop a three-dimensional analytical and computational basis for realistic modeling of behavior of rock masses under various loading conditions and physical effects (e.g. fluid flow, pore pressure). The goal is to create a computational model implemented in a general purpose code capable of accurate modeling of three-dimensional problems of multiple propagating fractures in piecewise homogeneous rocks that account for various loading conditions Rock mechanics applications may include hydraulic fracture problems characterized by coupling between the fracture mechanism and fluid flow. Thus, the code structure should allow for incorporation of coupled problems of this kind.

Significant features of the code include using MATLAB as the programming tool. MATLAB is a high-level language for numerical computations that features built-in linear algebra functions, graphics for data visualization, and could be easily integrated with external applications and languages. This would constitute a significant advantage over specific available Fortran-based codes.

The novel elements of the approach include the following:

- the use of complex variables to create various combinations of the fields, e.g. in-plane components of tractions, displacement discontinuities, as well as geometric parameters;
- analytical evaluation of complex integrals;
- enforcing the boundary conditions after the discretization and analytical handling of the internal fields, by allowing the field point to reach the boundaries.

The use of complex variables (e.g. the certain complex-valued combinations of the elastic fields) simplifies the analytical integration over the boundary elements and reduces the number of integral terms, as compared to real variables-based approaches. Since the limit (as the field point approaches the boundary) is taken after the approximation of the boundary and the unknown functions, no singular integrals are involved. Furthermore, there is no need for an additional procedure for evaluation of the elastic fields inside the domain; they are evaluated by the same procedure as the one used to set up the system of linear algebraic equations for the boundary unknowns. Analytical integration leads to higher accuracy of calculations and allows for saving computational time. In addition, it helps to facilitate the use of fast solving techniques, e.g. the Fast Multipole Method (see, e.g , Liu, 2009). The proposed mathematical model features triangular elements for boundary approximations and treatment of body forces via the equivalent boundary integrals.

3 Literature review

The problems of cracks and crack propagation in three-dimensional media have been first studied analytically. The analytical solutions of Sack (1946), Sneddon (1946), Green (1949), Segedin (1951), and Fabrikant (1987) were suggested for the problem of a penny-shaped crack in an infinite domain under different loading modes at infinity. Later on, the semi-analytical solutions for multiple penny-shaped cracks were proposed by several authors (see

Kushch, 1998, Kushch and Sangani, 1999). The problems of fracture of more complex geometry, as well as for multiple cracks, could only be solved numerically. BEM represents one of the most popular tools for solving Fracture Mechanics problems.

Boundary Element Method (BEM) is based on the boundary integral representation equivalent to the differential equation governing a specific physical problem. Such representation is possible when the so-called fundamental solution of the governing differential equation is available. The fundamental solution satisfies the differential equation everywhere in the domain except one point where it is singular. In the case of linear isotropic and homogeneous elasticity, the fundamental solution is that of a point force applied to an infinite domain, the so-called Kelvin's solution. Thus, (see Cruse, 1988), in the BEM, unlike in the Finite Element Method (FEM), the fields are already exactly self-equilibrated inside the computational domain, perhaps except for the boundary. This makes possible resolving high stress gradients and intrinsic singularities that are difficult to handle with FEM. Another significant feature of BEM is the absence of the volume mesh, which makes it possible to solve infinite medium problems. These features of BEM make it a powerful and versatile tool for various applications. The detailed description of the BEM formulations as well as the applications of the method can be found in various books (e.g. Gaul et al. 2003; Aliabadi 2002; Wrobel 2002; Cruse 1988). BEM is an efficient tool for solving fracture mechanics problems.

The BEM formulations for the fractures (see e.g. Aliabadi, 2002) can be classified as follows:

- Multi-region method (Lachat and Watson) that consists in subdividing the domain along the crack surface to create two artificial subdomains for each crack. In this procedure, displacement continuity and equilibrium of tractions are enforced across the artificial boundaries of the subdomains. The need to create additional boundaries leads to increase in computational costs and makes the method inefficient for multiple cracks.

- Dual BEM (Aliabadi) that consists in separate treatment of each side of the crack; the displacement integral equation is applied on one side of the crack and the tracton integral equation is applied on the other side. This also leads to increase in computational costs related to extra unknowns (displacements on each side of the crack are used).

- Displacement Discontinuity method (Crouch 1976) that consists in representing a crack by a set of displacement discontinuity elements. Knowing the analytical solution for the fields for a single element, the numerical solutions for those in the computational domain can be obtained by the standard superposition. Mathematically, this method is equivalent to the solution of a hypersingular integral equation with displacement discontinuity being the unknown density function. This approach requires a rigorous treatment of hypersingular integrals.

Although most BEM-based papers dealt with two-dimensional fractures, three-dimensional solutions are also available, e.g. Bui (1977), Weaver (1977), Lin'kov and Mogilevskaya (1986), Luchi and Rizzuti (1987), Kuriyama and Mizuta (1993), Chen and Gross (1997), Chen and Lee (2001), Frangi et al. (2002), Lo et al. (2005). There are also various papers on three-dimensional crack propagation, e.g. Mi and Aliabadi (1994), Kolk et al. (2005), Meng et al. (2013). Comprehensive lists of references on three-dimensional fracture problems could be found in the books by Cruse (1988) and Aliabadi (2002).

However, the results reported in the cited papers were related to the problems of fractures in homogeneous medium and simple loading conditions. The computational model that would include treatment of inhomogeneities, propagating cracks of arbitrary shape under complex loading conditions incorporating physical effects (e.g. fluid flow, pore pressure, temperature gradient, etc.) is still lacking.

4 Preliminary work: Three dimensional modeling of fractured elastic solid using the Boundary Element Method

The preliminary work is limited to the elastostatic problems. However, it would constitute the core part of a compuational technique to model three-dimensional problems of multiple propagating fractures in piecewise homogeneous rocks, which is the long term goal of the ongoing research.

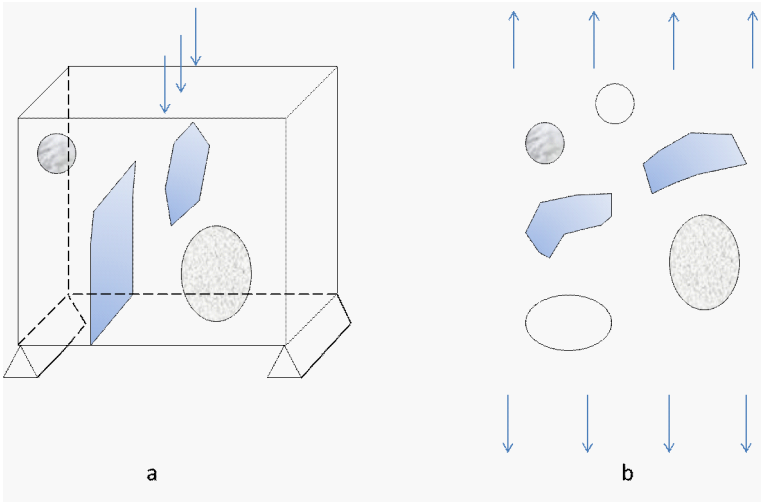

Figure 1: Problem formulation. Finite and infinite computational domain.

4.1 Problem formulation

Consider a finite or an infinite isotropic elastic domain characterized by the shear modulus μ and the Poisson's ratio ν and containing N fractures of arbitrary shapes (Fig.1 a,b). The load in the domain may be applied either locally (in the form of point forces), or via the boundaries of the domain including those of the fractures (in the form of boundary tractions). In case of an infinite domain, the load may be also applied via the far field stress. In addition, the medium could be subject to constant body forces (e.g. gravity). The load at the fractures' surfaces could be due to various physicals effects e.g. fluid pressure. The elastic fields inside of the domain are to be defined.

4.2 Basic equations

The governing differential equation for the problem is the Navier-Cauchy (Lamé) equilibrium equation of elasticity:

$$\lambda u_{k,ki} + \mu \left(u_{i,jj} + u_{j,ij} \right) + b_i = 0 \tag{1}$$

where $\lambda = 2\mu\nu / (1 - 2\nu)$ is Lamé constant of the medium, u_i and b_i $(i = 1 \dots 3)$ are the components of displacement vector $\mathbf{u}$, and body force vector $\mathbf{b}$, respectively. Here and in the following, standard indicial notation is used (i.e. repeated indices imply summation and $f_{,i} = \partial f / \partial x_i$). The fields in a finite domain can be alternatively represented by the integral expressions, the so-called Somigliana's identities.

4.2.1 Integral representations

The Somigliana's identity for displacements at a certain point x inside the elastic body has the following form:

$$u_i(x) = \int_{\partial\Omega} U_{ij}(x,\xi)\, t_j(\xi)\, dS_\xi + \int_{\partial\Omega} T_{ji}(\xi,x)\, u_j(\xi)\, dS_\xi + \int_{\Omega} U_{ij}(x,\eta)\, b_j dV_\eta \tag{2}$$

where Ω and $\partial\Omega$ indicate the domain and its boundary, t_j are the components of the traction vectors $\mathbf{t}$ at the point $\xi \in \partial\Omega$, $\eta \in \Omega$, U and T^T are the kernels of so-called single and double layer potentials that correspond to Kelvin's fundamental solution for displacements and tractions due to the point force applied at the point x (need ref.)

The tractions at the point x on the plane characterized by the normal vector $\mathbf{n}(x)$ can be obtained by appling Hooke's law to Eq. (2):

$$t_i(x) = \int_{\partial\Omega} T_{ij}(x,\xi)\, t_j(\xi)\, dS_\xi + \int_{\partial\Omega} H_{ij}(x,\xi)\, u_j(\xi)\, dS_\xi + \int_{\Omega} T_{ij}(x,\eta)\, b_j dV_\eta \tag{3}$$

where H is the so-called hypersingular kernel.

The components of the kernels U, T, and H denoted as $U_{ij}(x,\xi)$, $T_{ij}(x,\xi)$, and $H_{ij}(x,\xi)$ are as follows:

$$\begin{aligned}
U_{ij}(x,\xi) &= \frac{1}{16\pi(1-\nu)r}\left[(3-4\nu)\delta_{ij} + \frac{r_i r_j}{r^2}\right] \\
T_{ij}(x,\xi) &= \frac{1-2\nu}{8\pi(1-\nu)r^3}\left[n_i(x) r_j - r_k n_k(x)\delta_{ij} - r_i n_j(x)\right] - \frac{3}{8\pi(1-\nu)r^5} r_i r_k n_k(x) r_j \\
H_{ij}(x,\xi) &= -\mu\left\{\frac{1-2\nu}{4\pi(1-\nu)r^3}\left[n_k(x) n_k(\xi)\delta_{ij} + n_i(\xi) n_j(x)\right] - \frac{1-4\nu}{4\pi(1-\nu)r^3} n_i(x) n_j(\xi) + \right. \\
&\quad + \frac{3(1-2\nu)}{4\pi(1-\nu)r^5}\left[r_k n_k(\xi) n_i(x) r_j + r_k n_k(x) r_i n_j(\xi)\right] + \frac{3\nu}{4\pi(1-\nu)r^5} r_l n_l(\xi)\left[r_k n_k(x)\delta_{ij} + \right. \\
&\quad \left. + r_i n_j(x)\right] + \frac{3\nu}{4\pi(1-\nu)r^5} r_j\left[n_k(x) n_k(\xi) r_i + r_k n_k(x) n_i(\xi)\right] - \\
&\quad \left. - \frac{15}{4\pi(1-\nu)r^7} r_k n_k(x) r_l n_l(\xi) r_i r_j\right\}
\end{aligned}$$

where δ_{ij} is Kronecker's symbol, $r_k = x_k - \xi_k$ and $r = |x-\xi|$, $\mathbf{n}(\xi)$ is the outward normal at the point ξ.

For an infinite domain with cavities Eqs. (2) and (3) remain true under restrictions at infinity (regularity conditions) (see Aliabadi 2002). A fracture is treated as a cut (slot) of zero thickness. It can be represented by considering two adjacent subdomains with the fracture being the common part of the boundary. By summing up the traction identities for both sides of the fracture, one can obtain identities similar to Eqs. (2) and (3) with $\mathbf{u}$ substituted by the displacement discontinuity $\mathbf{\Delta u} = \mathbf{u}^+ - \mathbf{u}^-$ where " $+$ " and " $-$ " mean the opposite sides of the crack. Unlike in Multi-domain BEM, the conditions on the artificial boundaries (the boundaries complementary to the fracture surfaces) are prescribed in such a way that the integrals over these complementary boundaries cancel out in the process of summation and those boundaries do not need to be discretized. For a single crack, a similar identity could be obtained using the indirect formulation with hypersingular kernel; in this case the unknown density function could be shown to coinside with $\mathbf{\Delta u}$ (see Aliabadi 2002).

For the external boundaries where $\mathbf{n}$ is an outward normal (note that $\mathbf{n}$ should point inside the cavities if any are present), one may assume that $\mathbf{\Delta u} = \mathbf{u}^+ = \mathbf{u}$ and $\mathbf{u}^- = 0$. The direction of the normal for the fracture (that is perceived as a cut) may be chosen arbitrarily. This direction indicates the outward normal for the " $+$ " side and the inward one for the " $-$ " side of the crack. In the following, Eqs. (2) and (3) are used for the fracture with $\mathbf{u} = \mathbf{u}^+ - \mathbf{u}^-$.

4.2.2 Treatment of body integrals

The volume integrals representinbg the constant body force $\mathbf{b}$ are treated by the standard technique based on the following Galerkin vector representation:

$$U_{ik} = G_{ik,ll} - \frac{1}{2(1-\nu)} G_{il,lk}$$

Using the divergence theorem the volume integrals in Eqs.(2) and (3) are transformed to the following surface integrals:

$$\int\limits_{\Omega} U_{ij}(x,\xi)\, b_j dV_\xi = \int\limits_{\partial\Omega} P_i(\xi)\, dS_\xi$$
$$\int\limits_{\Omega} T_{ij}(x,\xi)\, b_j dV_\xi = \int\limits_{\partial\Omega} B_{ij}(\xi)\, n_j(x)\, dS_\xi$$

where

$$P_i(\xi) = \frac{1}{8\pi\mu}\left[b_i n_k(\xi)\, r_{,k} - \frac{1}{2(1-\nu)} b_k n_i(\xi)\, r_{,k}\right] \tag{4}$$
$$B_{ij}(\xi) = \frac{1}{8\pi(1-\nu)\, r}\delta_{ij}\left[(b_k n_k(\xi) - b_k r_{,k} n_l(\xi)\, r_{,l})\right] + \frac{1-2\nu}{16\pi(1-\nu)\, r}\left[(b_i n_j(\xi) + b_j n_i(\xi))\right] -$$
$$- \frac{1}{8\pi r} n_k(\xi)\, r_{,k}\left[b_i r_{,j} + b_j r_{,i}\right] + \frac{1}{16\pi(1-\nu)\, r} b_k r_{,k}\left[n_i(\xi)\, r_{,j} + n_j(\xi)\, r_{,i}\right]$$

Here $r_{,k} = \dfrac{r_k}{r}$; $r_k = x_k - \xi_k$; $r = |x-\xi|$. Thus,

$$t_i(x) = \int\limits_{\partial\Omega} T_{ij}(x,\xi)\, t_j(\xi)\, dS_\xi + \int\limits_{\partial\Omega} H_{ij}(x,\xi)\, u_j(\xi)\, dS_\xi + \int\limits_{\partial\Omega} B_{ij}(\xi)\, n_j(x)\, dS_\xi \tag{5}$$

4.3 Numerical solution

4.3.1 Basic assumptions

In the present work, the boundaries are approximated by a set of planar triangular elements. Up to date, the piecewise constant approximations of the boundary unknowns are employed. The approximations of the higher order would be used in the future research.

For each boundary element, the following "local" cartesian coordinate system is introduced (Fig. 2). The basis vector $\widehat{\mathbf{e}}_1$ of the system is chosen to be parallel to the edge between the two vertices of the element. The basis vector $\widehat{\mathbf{e}}_3$ is chosen to be equal to $-\mathbf{n}$, and the basis vector $\widehat{\mathbf{e}}_2 = \widehat{\mathbf{e}}_3 \times \widehat{\mathbf{e}}_1$ is chosen in such a way that the basis $\widehat{\mathbf{e}}_1\widehat{\mathbf{e}}_2\widehat{\mathbf{e}}_3$ is right-handed. In the following subsections the contribution of the element E_ξ to the fields at some internal point x will be considered. It is convenient to set the origin of the local coordinate system at the point x', which is defined as the projection of the field point x onto the element's plane.

The boundary unknowns will be defined from the system of algebraic equations set up to satisfy the boundary conditions at the defined set of points (collocaion points). Due to the use of constant approximations, the centers of the triangles are the natural choice for the collocation points.

4.3.2 Complex variable notations

Let us introduce the following complex combinations of traction and displacement components, as well as the representation of a source point $\xi \in E_\xi$:

$$\begin{aligned} \underline{t} &= t_1 + i t_2; \qquad t_{\mathbf{n}} = t_3 \\ \underline{u} &= u_1 + i u_2; \qquad u_{\mathbf{n}} = u_3 \\ z &= (\xi_1 - x_1) + i(\xi_2 - x_2); \quad h = \xi_3 - x_3 \end{aligned} \tag{6}$$

Consider a plane containing the point x and characteraised by the normal vector $\mathbf{n}(x)$ and introduce the following complex combination of in-plane components of $\mathbf{n}(x)$:

$$\underline{n}(x) = n_1(x) + i n_2(x); \qquad n_{\mathbf{n}} = n_3$$

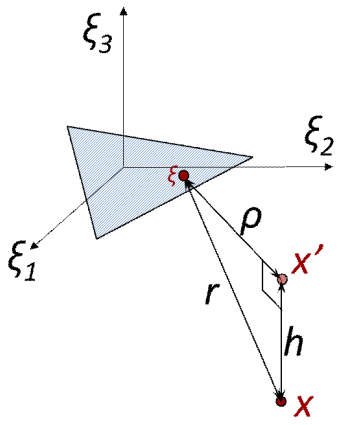

Figure 2: Boundary element. Local coordinate system.

The surface area element dS_ξ can be expressed as follows:

$$dS_\xi = -\frac{i}{4}\frac{\overline{z}}{z} d\left(z\overline{z}\right) d\left(\frac{z}{\overline{z}}\right) = -\frac{i}{4\zeta^2} d\rho^2 d\zeta^2$$

where $\overline{z}$ is the complex conjugate of z and new independent complex variables, ρ and ζ are as follows:

$$\rho = |z|\,; \quad \zeta^2 = \frac{z}{\overline{z}}; \quad z = \rho\zeta; \quad \overline{z} = \frac{\rho}{\zeta}$$

Now let us express tangential and normal components of the traction at the point x in terms of ρ and ζ, assuming that $\mathbf{u}$ and $\mathbf{t}$ are constant on the surface element ($\mathbf{b}$ is assumed constant in the domain). For the stress components associated with out-of-plane component of normal $n_{\mathbf{n}}(x)$ one has

$$\begin{aligned}
\underline{t}^{(\mathbf{n})}(x) = \sigma_{13}(x) + i\sigma_{23}(x) = \qquad (7)\\
\frac{i\mu}{32\pi(1-\nu)}\Big\{\underline{u}\left((\nu-2)\mathbf{I}_{022} - 3\nu h^2\mathbf{I}_{023} + 15h^2\mathbf{I}_{224}\right)\\
-\overline{u}\left(3\nu\mathbf{I}_{203} - 15h^2\mathbf{I}_{204}\right) + u_{\mathbf{n}}\left(6h\mathbf{I}_{113} - 30h^3\mathbf{I}_{114}\right)\Big\}\\
+\frac{i}{64\pi(1-\nu)}\Big\{2(1-2\nu)\left(\underline{t}h\mathbf{I}_{022} - t_{\mathbf{n}}\mathbf{I}_{112}\right) - 3\left(\overline{t}h\mathbf{I}_{203} + \underline{t}h\mathbf{I}_{223} - 2t_{\mathbf{n}}h^2\mathbf{I}_{113}\right)\Big\} -\\
-\frac{i}{64\pi(1-\nu)}\left\{(1-2\nu)\left(\underline{b}\mathbf{I}_{021} + b_{\mathbf{n}}h\mathbf{I}_{112}\right) + 2(1-\nu)\underline{b}h^2\mathbf{I}_{022} + \frac{1}{2}\left(\overline{b}\mathbf{I}_{202} + \underline{b}\mathbf{I}_{222}\right)\right\}
\end{aligned}$$

$$\begin{aligned}
t_{\mathbf{n}}^{(\mathbf{n})}(x) = \sigma_{33}(x) = \qquad (8)\\
\frac{i\mu}{32\pi(1-\nu)}\Big\{\underline{u}\left(3h\mathbf{I}_{133} - 15h^3\mathbf{I}_{134}\right) + \overline{u}\left(3h\mathbf{I}_{113} - 15h^3\mathbf{I}_{114}\right)\\
+u_{\mathbf{n}}\left(2\mathbf{I}_{022} - 12h^2\mathbf{I}_{023} - 30h^4\mathbf{I}_{024}\right)\Big\}\\
+\frac{i}{64\pi(1-\nu)}\Big\{(1-2\nu)\left(\overline{t}h\mathbf{I}_{112} + \underline{t}\mathbf{I}_{132} + 2t_{\mathbf{n}}h\mathbf{I}_{022}\right) - 3\left(\overline{t}h^2\mathbf{I}_{113} + \underline{t}h^2\mathbf{I}_{133} - 2t_{\mathbf{n}}h^3\mathbf{I}_{023}\right)\Big\} +\\
+\frac{i}{64\pi(1-\nu)}\Big\{(1-\nu)\left(\overline{b}h\mathbf{I}_{112} + \underline{b}h\mathbf{I}_{132} - 2b_{\mathbf{n}}\mathbf{I}_{021}\right) + 2(1+\nu)b_{\mathbf{n}}h^2\mathbf{I}_{022}\Big\}
\end{aligned}$$

where $\overline{u}$, $\overline{t}$, and $\overline{b}$ are the complex conjugate of $\underline{u}$, $\underline{t}$, and $\underline{b}$, respectively.

For the other three components of the stress tensor associated with in-plane components of $\mathbf{n}$, one has

$$
\begin{aligned}
\underline{t}^{(\mathbf{p})}(x) \;=\; & \left(\sigma_{11}(x)+\sigma_{22}(x)\right)\underline{n}(x)+\left(\sigma_{11}(x)-\sigma_{22}(x)+i\sigma_{12}(x)\right)\overline{n}(x)= \\
& \frac{i\mu}{16\pi(1-\nu)}\left\{\underline{n}(x)\left[\underline{u}\left(\frac{3}{2}(1-\nu)\,h\mathbf{I}_{133}-\frac{15}{4}h\mathbf{I}_{334}\right)\right.\right. \\
& \qquad +\overline{u}\left(\frac{3}{2}(1-\nu)\,h\mathbf{I}_{113}-\frac{15}{4}h\mathbf{I}_{314}\right) \\
& \qquad \left.+u_{\mathbf{n}}\left((1-4\nu)\,\mathbf{I}_{022}-\frac{3}{2}(1-2\nu)\left(h^2\mathbf{I}_{023}+\mathbf{I}_{223}\right)+\frac{15}{2}h^2\mathbf{I}_{224}\right)\right] \\
& \quad +\overline{n}(x)\left[\underline{u}\left(3\nu h\mathbf{I}_{113}-\frac{15}{4}h\mathbf{I}_{314}\right)+\overline{u}\left(-\frac{15}{4}h\mathbf{I}_{3-14}\right)\right. \\
& \qquad \left.\left.+u_{\mathbf{n}}\left(-\frac{3}{2}(1-2\nu)\,h\mathbf{I}_{203}+\frac{15}{2}h^2\mathbf{I}_{204}\right)\right]\right\} \\
& +\frac{i}{64\pi(1-\nu)}\left\{\underline{n}(x)\left[2(1-2\nu)\,t_{\mathbf{n}}h\mathbf{I}_{022}-\frac{3}{2}\left(\overline{t}\mathbf{I}_{313}+\underline{t}\mathbf{I}_{333}+2t_{\mathbf{n}}h\mathbf{I}_{223}\right)\right]\right. \\
& \qquad \left.+\overline{n}(x)\left[-2(1-2\nu)\,\underline{t}\mathbf{I}_{112}-\frac{3}{2}\left(\overline{t}\mathbf{I}_{3-13}+\underline{t}\mathbf{I}_{313}+2t_{\mathbf{n}}h\mathbf{I}_{203}\right)\right]\right\} \\
& +\frac{i}{64\pi(1-\nu)}\left\{\underline{n}(x)\left[\nu b_{\mathbf{n}}\left(\mathbf{I}_{011}-2h^2\mathbf{I}_{012}\right)-(1+\nu)\,h\left(\overline{b}\mathbf{I}_{102}+\underline{b}\mathbf{I}_{122}\right)\right]\right. \\
& \qquad \left.+\overline{n}(x)\left[-2h\underline{b}\mathbf{I}_{102}\right]\right\}
\end{aligned}
\tag{9}
$$

where $\overline{n}(x)$ is the complex conjugate of $\underline{n}(x)$.

Integrals $\mathbf{I}_{ijk}$ involved in Eqs. (7) - (9) are of the following general form

$$
\mathbf{I}_{ijk}=\sum_{\substack{m,n=1\\ n=(m+1)\bmod 3}}^{3}\int_{\zeta_m^2}^{\zeta_n^2}\int_{0}^{\rho^2(\zeta)}\frac{\rho^i}{\zeta^j r^{2k-1}}d\rho^2 d\zeta^2 \tag{10}
$$

where i,j,and k are integer numbers.

The limits of integration in Eq. (10) are the same for all terms and determined by the shape of the boundary element E_ξ. For a planar triangular element it is easy to perform integration separately for each edge. Due to the fact that ρ on every edge is easily expressed through $\zeta=e^{i\arg z}$, the integration over ρ between the origin x' and an edge is performed first. After the second integration over ζ, the contributions from all edges must be added together.

4.3.3 Integrals in complex notations

All integrals involved in Eqs. (7) - (9) have the common form (10). There is no need, however, to directly evaluate all of the integrals because most of them could be found by the differentiation of the basic integrals with respect to the parameter h defined in Eq. (6) (see the following subsections). It is natural to express each of the basic integrals as the sum of three integrals associated with each edge of the triangle:

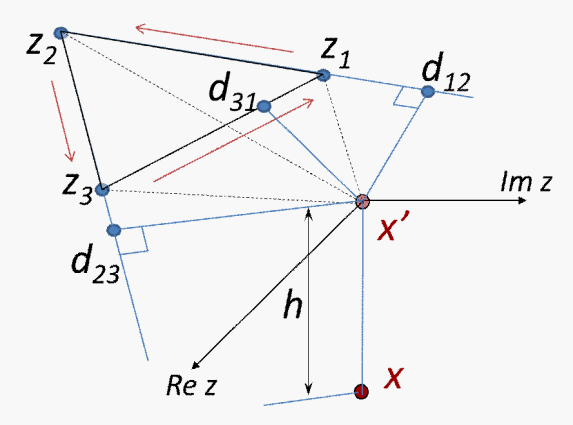

Figure 3: Integration scheme. Complex notations.

$$
\begin{aligned}
\mathbf{I}_{021} &= \sum_{m,n=1}^{3} I_{mn}^{(1)}; \qquad I_{mn}^{(1)} = \int_{\zeta_m^2}^{\zeta_n^2} \int_{0}^{\rho^2(\zeta)} \frac{1}{\zeta^2 r} d\rho^2 d\zeta^2 \\
\mathbf{I}_{112} &= \sum_{m,n=1}^{3} I_{mn}^{(2)}; \qquad I_{mn}^{(2)} = \int_{\zeta_m^2}^{\zeta_n^2} \int_{0}^{\rho^2(\zeta)} \frac{\rho}{\zeta r^3} d\rho^2 d\zeta^2 \\
\mathbf{I}_{132} &= \sum_{m,n=1}^{3} I_{mn}^{(3)}; \qquad I_{mn}^{(3)} = \int_{\zeta_m^2}^{\zeta_n^2} \int_{0}^{\rho^2(\zeta)} \frac{\rho}{\zeta^3 r^3} d\rho^2 d\zeta^2 \\
\mathbf{I}_{202} &= \sum_{m,n=1}^{3} I_{mn}^{(4)}; \qquad I_{mn}^{(4)} = \int_{\zeta_m^2}^{\zeta_n^2} \int_{0}^{\rho^2(\zeta)} \frac{\rho^2}{r^3} d\rho^2 d\zeta^2 \\
\mathbf{I}_{222} &= \sum_{m,n=1}^{3} I_{mn}^{(5)}; \qquad I_{mn}^{(5)} = \int_{\zeta_m^2}^{\zeta_n^2} \int_{0}^{\rho^2(\zeta)} \frac{\rho^2}{\zeta^2 r^3} d\rho^2 d\zeta^2 \\
\mathbf{I}_{3-12} &= \sum_{m,n=1}^{3} I_{mn}^{(6)} \qquad I_{mn}^{(6)} = \int_{\zeta_m^2}^{\zeta_n^2} \int_{0}^{\rho^2(\zeta)} \frac{\rho^3 \zeta}{r^3} d\rho^2 d\zeta^2 \\
\mathbf{I}_{312} &= \sum_{m,n=1}^{3} I_{mn}^{(7)} \qquad I_{mn}^{(7)} = \int_{\zeta_m^2}^{\zeta_n^2} \int_{0}^{\rho^2(\zeta)} \frac{\rho^3}{\zeta r^3} d\rho^2 d\zeta^2 \\
\mathbf{I}_{332} &= \sum_{m,n=1}^{3} I_{mn}^{(8)} \qquad I_{mn}^{(8)} = \int_{\zeta_m^2}^{\zeta_n^2} \int_{0}^{\rho^2(\zeta)} \frac{\rho^3}{\zeta^3 r^3} d\rho^2 d\zeta^2
\end{aligned}
\tag{11}
$$

where indices m and n denote the vertices of the triangle and $n = (m+1) \bmod 3$. Thus, the order in the subscript indices reflects the order of integration along the perimeter of the triangle, i.e 1 to 2, 2 to 3, 3 to 1.

The parameter h is involved in Eqs. (10) via the expression for r. Neither of the integration variables (ρ and ζ), nor the integration limits depend on h. Thus, one can directly differentiate Eqs. (11) with respect to h under the integral sign. Thus, for any i and j, other integrals can be found via recursive formulae

$$\mathbf{I}_{ij2} = -2\frac{\partial}{\partial\left(h^2\right)}\mathbf{I}_{ij1}; \qquad \mathbf{I}_{ij3} = -\frac{2}{3}\frac{\partial}{\partial\left(h^2\right)}\mathbf{I}_{ij2} = \frac{4}{3}\frac{\partial^2}{\partial\left(h^2\right)^2}\mathbf{I}_{ij1} \tag{12}$$
$$\mathbf{I}_{ij4} = -\frac{2}{5}\frac{\partial}{\partial\left(h^2\right)}\mathbf{I}_{ij3} = \frac{4}{15}\frac{\partial^2}{\partial\left(h^2\right)^2}\mathbf{I}_{ij2} = -\frac{8}{15}\frac{\partial^3}{\partial\left(h^2\right)^3}\mathbf{I}_{ij1}$$

The detail on analytical integration of basic terms can be found in the following subsection.

4.3.4 Analytical expressions for the basic integrals

As could be clearly seen, the integration variables are separated in each term, and the integration over ρ^2 is performed first.

This integration involves only the following four types of integrands.

$$\int_0^{\rho^2(\zeta)} \frac{1}{r} d\rho^2 = 2r\left(\zeta\right) - 2h$$
$$\int_0^{\rho^2(\zeta)} \frac{\rho}{r^3} d\rho^2 = -2\left[\frac{\rho\left(\zeta\right)}{r\left(\zeta\right)} + i\arctan\left(i\frac{\rho\left(\zeta\right)}{r\left(\zeta\right)}\right)\right]$$
$$\int_0^{\rho^2(\zeta)} \frac{\rho^2}{r^3} d\rho^2 = 2\left[r\left(\zeta\right) + \frac{h^2}{r\left(\zeta\right)} - 2h\right]$$
$$\int_0^{\rho^2(\zeta)} \frac{\rho^3}{r^3} d\rho^2 = \rho\left(\zeta\right) r\left(\zeta\right) + 2h^2\frac{\rho\left(\zeta\right)}{r\left(\zeta\right)} - 3ih^2\arctan\left(\frac{i\rho\left(\zeta\right)}{r\left(\zeta\right)}\right)$$

Here $r\left(\zeta\right) = \sqrt{\rho^2\left(\zeta\right) + h^2}$ and $\rho\left(\zeta\right)$ is given by the following equation of a straight line:

$$\rho\left(\zeta\right) = \frac{2\left|d^{(mn)}\right|}{\frac{\zeta}{\widehat{d}^{(mn)}} + \frac{\widehat{d}^{(mn)}}{\zeta}} \tag{13}$$

where $\underline{d}^{(mn)} = \left|d^{(mn)}\right|\widehat{d}^{(mn)}$ is related to the vector perpendicular to the line passing through m-th and n-th vertices starting from the origin (x') (see Fig. 3).

Integrating over ζ along some edge involves the following integrals (Gradsteyn and Ryzhik, 2000):

$$J_1 = \int_{u_m}^{u_n} \frac{du}{u\sqrt{R\left(2\underline{d}u - \widehat{d}^2\right)}} = \frac{1}{\widehat{d}}\arctan\left.\frac{\left(\zeta^2 - \widehat{d}^2\right)}{2\widehat{d}\sqrt{R\left(\zeta\right)}}\right|_{\zeta_m}^{\zeta_n}; \qquad u_k = \frac{1}{2\left|d\right|}\left(\frac{\zeta_k^2}{\widehat{d}} + \widehat{d}\right)$$
$$J_2 = \int_{\zeta_m^2}^{\zeta_n^2} \frac{d\zeta^2}{\sqrt{R(\zeta)}} = \frac{2\underline{d}}{h}\ln\left.\left(\frac{h}{\underline{d}}\sqrt{R\left(\zeta\right)} + \frac{h^2}{2\underline{d}^2}\zeta^2 + \frac{h^2}{2\left|d\right|^2} + 1\right)\right|_{\zeta_m}^{\zeta_n}$$
$$J_3 = \int_{\zeta_m^2}^{\zeta_n^2} \frac{d\zeta^2}{\zeta^2\sqrt{R(\zeta)}} = -\frac{2d^*}{h}\ln\left.\frac{\frac{h}{d^*}\sqrt{R\left(\zeta\right)} + \left(1 + \frac{h^2}{2|d|^2}\right)\zeta^2 + \frac{h^2}{2d^{*2}}}{\zeta^2}\right|_{\zeta_m}^{\zeta_n}$$

$$\begin{aligned}
\int_{w_m}^{\zeta_n^2} \arctan\left(\frac{i\zeta}{\sqrt{R(\zeta)}}\right)\frac{d\zeta^2}{\zeta} &= 2\zeta \arctan\frac{i\zeta}{\sqrt{R(\zeta)}}\Bigg|_{\zeta_m}^{\zeta_n} + iJ_2 - 2i\widehat{d}^2 J_1 \\
\int_{\zeta_m^2}^{\zeta_n^2} \arctan\left(\frac{i\zeta}{\sqrt{R(\zeta)}}\right)\frac{d\zeta^2}{\zeta^3} &= \frac{2}{\zeta}\arctan\frac{i\zeta}{\sqrt{R(\zeta)}}\Bigg|_{\zeta_m}^{\zeta_n} - iJ_3 + 2iJ_1
\end{aligned}$$

where

$$R(\zeta) = \frac{r^2(\zeta)}{\rho^2(\zeta)}\zeta^2 = \zeta^2 + \frac{h^2}{4\left|d^{(mn)}\right|^2}\left(\frac{\zeta^2}{\widehat{d}} + \widehat{d}^{(mn)}\right)^2 = \frac{h^2}{4\overline{d^{(mn)}}^2} + \left(\frac{h^2}{2\left|d^{(mn)}\right|^2} + 1\right)\zeta^2 + \frac{h^2}{4\underline{d}^{(mn)2}}\zeta^4$$

Note that

$$\frac{\left(\zeta^{(k)2} - \widehat{d}^{(mn)2}\right)}{2\widehat{d}^{(mn)}\sqrt{R\left(\zeta^{(k)}\right)}} = \frac{\rho^{(k)}}{2r^{(k)}}\left(\frac{\zeta^{(k)}}{\widehat{d}^{(mn)}} - \frac{\widehat{d}^{(mn)}}{\zeta^{(k)}}\right) = \frac{i\rho^{(k)}\sin\left(\arg z^{(k)} - \arg\underline{d}^{(mn)}\right)}{r^{(k)}} = \frac{ia^{(kmn)}}{r^{(k)}}$$

(see the notations below). Finally, the closed form expressions for $I_{mn}^{(1)} - I_{mn}^{(8)}$ are

$$\begin{aligned}
I_{mn}^{(1)} &= 4\left[\left|d^{(mn)}\right| H_0^{(kmn)}(h) + i|h|\left(G_0^{(kmn)}(h) - \chi^{(kmn)}\right)\right]_{k=m}^{k=n} \\
I_{mn}^{(2)} &= -4\left[\widehat{d}^{(mn)} H_0^{(kmn)}(h) + i\zeta^{(k)} J_0^{(kmn)}(h)\right]_{k=m}^{k=n} \\
I_{mn}^{(3)} &= 4\left[\frac{i}{\zeta^{(k)}} J_0^{(kmn)}(h) - \frac{1}{\widehat{d}^{(mn)}} H_0^{(kmn)}(h)\right]_{k=m}^{k=n} = -\overline{I_{mn}^{(2)}} \\
I_{mn}^{(4)} &= 4\left[2\frac{\underline{d}^{(mn)} r^{(k)}\zeta^{(k)}}{\rho^{(k)}} - \left|d^{(mn)}\right|\widehat{d}^{(mn)2} H_0^{(kmn)}(h)\right]_{k=m}^{k=n} \\
I_{mn}^{(5)} &= 4\left[\left|d^{(mn)}\right| H_0^{(kmn)}(h) + 2i|h|\left(G_0^{(kmn)}(h) - \chi^{(kmn)}\right)\right]_{k=m}^{k=n} \\
I_{mn}^{(6)} &= 2\left[-\widehat{d}^{(mn)3}\left(h^2 + 3\left|d^{(mn)}\right|^2\right) H_0^{(kmn)}(h)\right. \\
&\qquad \left. + \left|d^{(mn)}\right|\widehat{d}^{(mn)3} r^{(k)}\left(1 + 4K_0^{(kmn)}\right)\right]_{k=m}^{k=n} \\
I_{mn}^{(7)} &= 2\left[\widehat{d}^{(mn)}\left(3h^2 + \left|d^{(mn)}\right|^2\right) H_0^{(kmn)}(h) - \underline{d}^{(mn)} r^{(k)}\right]_{k=m}^{k=n} \\
I_{mn}^{(8)} &= 2\left[\frac{1}{\widehat{d}^{(mn)}}\left(3h^2 + \left|d^{(mn)}\right|^2\right) H_0^{(kmn)}(h) + \overline{d}^{(mn)} r^{(k)}\right]_{k=m}^{k=n} = -\overline{I_{mn}^{(7)}}
\end{aligned} \tag{14}$$

where

$$
\begin{aligned}
G_0^{(kmn)}(h) &= \arctan\left(\frac{|h|}{r^{(k)}}\tan\chi^{(kmn)}\right), \quad \chi^{(kmn)} = \arg z^{(k)} - \arg \underline{d}^{(mn)} \\
H_0^{(kmn)}(h) &= \arctan\frac{ia^{(kmn)}}{r^{(k)}}, \qquad\qquad a^{(kmn)} = \rho^{(k)}\sin\chi^{(kmn)} \\
J_0^{(kmn)}(h) &= \arctan\frac{i\rho^{(k)}}{r^{(k)}}, \qquad\qquad r^{(k)} = \sqrt{\rho^{(k)2} + h^2} \\
K_0^{(kmn)} &= e^{i\chi^{(kmn)}}\cos\chi^{(kmn)}
\end{aligned}
$$

The expressions (14) need to be summed up over all edges of the triangle (11).

4.3.5 Evaluation of the remaining integrals

The rest of the integral terms can be evaluated using Eq. (12). The expressions for the derivatives of G_0, H_0, and J_0 are as follows:

$$
\begin{aligned}
G_1^{(kmn)}(h) &= \frac{\partial}{\partial(h^2)}G_0^{(kmn)}(h) = \frac{|h|}{r^{(k)}}\Psi\tan\chi^{(kmn)} \qquad (15)\\
G_2^{(kmn)}(h) &= \frac{\partial^2}{\partial(h^2)^2}G_0^{(kmn)}(h) = \frac{|h|}{r^{(k)}}\left[-2\Psi^2 + \left(1 + \frac{h^2}{r^{(k)2}}\right)\Psi\right]\tan\chi^{(kmn)} \\
G_3^{(kmn)}(h) &= \frac{\partial^3}{\partial(h^2)^3}G_0^{(kmn)}(h) = \frac{|h|}{r^{(k)}}\left[4\Psi^3 - \left(7 + 2\frac{h^2}{r^{(k)2}}\right)\Psi^2 + \frac{3}{2}\left(1 + \frac{h^2}{r^{(k)2}} + \frac{h^4}{r^{(k)4}}\right)\Psi\right]\tan\chi^{(kmn)} \\
H_1^{(kmn)}(h) &= \frac{\partial}{\partial(h^2)}H_0^{(kmn)}(h) = -\frac{i}{2}\frac{a^{(kmn)}}{r^{(k)}}\Phi \\
H_2^{(kmn)}(h) &= \frac{\partial^2}{\partial(h^2)^2}H_0^{(kmn)}(h) = \frac{i}{4}\frac{a^{(kmn)}}{r^{(k)}}\Phi^2\left(3 - \frac{a^{(kmn)2}}{r^{(k)2}}\right) \\
H_3^{(kmn)}(h) &= \frac{\partial^3}{\partial(h^2)^3}H_0^{(kmn)}(h) = -\frac{i}{8}\frac{a^{(kmn)}}{r^{(k)}}\Phi^3\left(15 - 10\frac{a^{(kmn)2}}{r^{(k)2}} + 3\frac{a^{(kmn)4}}{r^{(k)4}}\right) \\
J_1^{(kmn)}(h) &= \frac{\partial}{\partial(h^2)}J_0^{(kmn)}(h) = -\frac{i\rho^{(k)}}{2h^2r^{(k)}}; \quad J_2^{(kmn)}(h) = \frac{\partial^2}{\partial(h^2)^2}J_0^{(kmn)}(h) = \frac{i\rho^{(k)}}{4h^4r^{(k)}}\left(2 + \frac{h^2}{r^{(k)2}}\right)
\end{aligned}
$$

where

$$
\Psi = \frac{\rho^{(k)2}}{r^{(k)2} + h^2\tan^2\chi^{(kmn)}}, \quad \Phi = \frac{1}{r^{(k)2} - a^{(kmn)2}} = \frac{1}{h^2 + \left|d^{(mn)}\right|^2}
$$

It is convenient to introduce the following notations:

$$
\begin{aligned}
\widetilde{G}_s^{(kmn)}(h) &= \frac{1}{|h|}\frac{\partial^s}{\partial(h^2)^s}G_0^{(kmn)}(h), \quad \widetilde{J}_s^{(kmn)}(h) = -i\frac{\partial^s}{\partial(h^2)^s}J_0^{(kmn)}(h), \quad s = 1\ldots3 \qquad (16)\\
\widetilde{H}_1^{(kmn)}(h) &= 2i\frac{\partial}{\partial(h^2)}H_0^{(kmn)}(h) = \frac{a^{(kmn)}}{r^{(k)}}\Phi \\
\widetilde{H}_2^{(kmn)}(h) &= -4i\frac{\partial^2}{\partial(h^2)^2}H_0^{(kmn)}(h) = \frac{a^{(kmn)}}{r^{(k)}}\Phi^2\left(3 - \frac{a^{(kmn)2}}{r^{(k)2}}\right) \\
\widetilde{H}_3^{(kmn)}(h) &= 8i\frac{\partial^3}{\partial(h^2)^3}H_0^{(kmn)}(h) = \frac{a^{(kmn)}}{r^{(k)}}\Phi^3\left(15 - 10\frac{a^{(kmn)2}}{r^{(k)2}} + 3\frac{a^{(kmn)4}}{r^{(k)4}}\right)
\end{aligned}
$$

4.3.6 Expressions for the stresses (for hypersingular kernel)

The basic integrals and their derivatives can be substituted to Eqs. (7) - (9) to find the stress or traction components at the point x. It should be noted that the terms containing only vertex coordinates $\rho^{(k)}$, $r^{(k)}$, and $\zeta^{(k)}$ and not containing $a^{(kmn)}$, or $\underline{d}^{(mn)}$, or $\chi^{(kmn)}$ eventually cancel out after the summation over the perimeter of the triangle (thus, the terms with J_1 and J_2 can be omitted). This holds true for any value of h. Finally, for the stress tensor components in the coordinate systrem associated with the element E_ξ, one has

$$\begin{aligned}
&\sigma_{11}(x)+\sigma_{22}(x)= \qquad (17)\\
&\frac{\mu}{4\pi(1-\nu)}\sum_{m,n=1}^{3}\left[\underline{u}\left(-\frac{1}{8}\frac{i}{\widehat{d}^{(mn)}}\frac{h\left|d^{(mn)}\right|}{r^{(k)3}}+\frac{\nu+2}{2}\frac{h}{\widehat{d}^{(mn)}}\widetilde{H}_1^{(kmn)}(h)\right.\right.\\
&\qquad\left.-\frac{1}{8}\frac{h}{\widehat{d}^{(mn)}}\left(3h^2+\left|d^{(mn)}\right|^2\right)\widetilde{H}_2^{(kmn)}(h)\right)\\
&\quad+\overline{u}\left(\frac{1}{8}i\widehat{d}^{(mn)}\frac{h\left|d^{(mn)}\right|}{r^{(k)3}}+\frac{\nu+2}{2}h\widehat{d}^{(mn)}\widetilde{H}_1^{(kmn)}(h)\right.\\
&\qquad\left.-\frac{1}{8}h\widehat{d}^{(mn)}\left(3h^2+\left|d^{(mn)}\right|^2\right)\widetilde{H}_2^{(kmn)}(h)\right)\\
&\quad+u_{\mathbf{n}}\left(-2\nu\widetilde{G}_1^{(kmn)}(h)+2\nu\widetilde{G}_2^{(kmn)}(h)\right.\\
&\qquad\left.\left.-\frac{1-6\nu}{2}\left|d^{(mn)}\right|\widetilde{H}_1^{(kmn)}(h)+\frac{1-4\nu}{2}h^2\left|d^{(mn)}\right|\widetilde{H}_2^{(kmn)}(h)\right)\right]\Bigg|_{k=m}^{k=n}
\end{aligned}$$

$$\begin{aligned}
&\sigma_{11}(x)-\sigma_{22}(x)+i\sigma_{12}(x)= \qquad (18)\\
&\frac{\mu}{4\pi(1-\nu)}\sum_{m,n=1}^{3}\left[\underline{u}\left(\frac{1}{8}i\widehat{d}^{(mn)}\frac{h\left|d^{(mn)}\right|}{r^{(k)3}}+\frac{3-2\nu}{2}h\widehat{d}^{(mn)}\widetilde{H}_1^{(kmn)}(h)\right.\right.\\
&\qquad\left.-\frac{1}{8}h\widehat{d}^{(mn)}\left(3h^2+\left|d^{(mn)}\right|^2\right)\widetilde{H}_2^{(kmn)}(h)+2\nu h\zeta^{(k)}\widetilde{J}_1^{(kmn)}(h)\right)\\
&\quad+\overline{u}\left(-\frac{1}{2}h\widehat{d}^{(mn)3}\widetilde{H}_1^{(kmn)}(h)+\frac{1}{8}h\widehat{d}^{(mn)3}\left(h^2+3\left|d^{(mn)}\right|^2\right)\widetilde{H}_2^{(kmn)}(h)\right.\\
&\qquad\left.-\frac{i}{8}h\widehat{d}^{(mn)3}\frac{\left|d^{(mn)}\right|}{r^{(k)3}}\left(1+4K_0^{(kmn)}\right)\right)\\
&\quad+u_{\mathbf{n}}\left(\frac{2\nu-1}{2}\left|d^{(mn)}\right|\widehat{d}^{(mn)2}\widetilde{H}_1^{(kmn)}(h)+\frac{1}{2}\left|d^{(mn)}\right|\widehat{d}^{(mn)2}\widetilde{H}_2^{(kmn)}(h)\right.\\
&\quad\left.\left.+\left(1-2\nu-\frac{h^2}{r^{(k)2}}\right)\frac{\widehat{d}^{(mn)2}}{r^{(k)}}iK_0^{(kmn)}\right)\right]\Bigg|_{k=m}^{k=n}
\end{aligned}$$

$$\sigma_{33}(x) = \tag{19}$$
$$\frac{\mu}{4\pi(1-\nu)}\sum_{m,n=1}^{3}\left\{\underline{u}\left(-\frac{h}{2\widehat{d}^{(mn)}}\widetilde{H}_1^{(kmn)}(h)+\frac{h^3}{2\widehat{d}^{(mn)}}\widetilde{H}_2^{(kmn)}(h)\right)\right.$$
$$+\overline{u}\left(-\frac{h\widehat{d}^{(mn)}}{2}\widetilde{H}_1^{(kmn)}(h)+\frac{h^3\widehat{d}^{(mn)}}{2}\widetilde{H}_2^{(kmn)}(h)\right)$$
$$+u_{\mathbf{n}}\left[\widetilde{G}_1^{(kmn)}(h)-2\widetilde{G}_2^{(kmn)}(h)+2\widetilde{G}_3^{(kmn)}(h)\right.$$
$$\left.\left.\left.+\left|d^{(mn)}\right|\left(\widetilde{H}_1^{(kmn)}(h)+2h^2\widetilde{H}_2^{(kmn)}(h)-h^4\widetilde{H}_3^{(kmn)}(h)\right)\right]\right\}\Big|_{k=m}^{k=n}$$

$$\sigma_{13}(x)+i\sigma_{23}(x) = \tag{20}$$
$$\frac{\mu}{4\pi(1-\nu)}\sum_{m,n=1}^{3}\left\{\underline{u}\left(\frac{\nu-2}{2}\widetilde{G}_1^{(kmn)}(h)-\frac{\nu-2}{2}\widetilde{G}_2^{(kmn)}(h)\right.\right.$$
$$\left.-\frac{\nu-2}{2}\left|d^{(mn)}\right|\widetilde{H}_1^{(kmn)}(h)+\frac{\nu-1}{2}\left|d^{(mn)}\right|h^2\widetilde{H}_2^{(kmn)}(h)\right)$$
$$+\overline{u}\left(-\frac{\nu}{2}\left|d^{(mn)}\right|\widehat{d}^{(mn)2}\widetilde{H}_1^{(kmn)}(h)+\frac{1}{2}\left|d^{(mn)}\right|\widehat{d}^{(mn)2}h^2\widetilde{H}_2^{(kmn)}(h)\right.$$
$$\left.+\left(\nu-\frac{h^2}{r^{(k)2}}\right)\frac{\widehat{d}^{(mn)2}}{r^{(k)}}iK_0^{(kmn)}\right)$$
$$u_{\mathbf{n}}\left(-h\widehat{d}^{(mn)}\widetilde{H}_1^{(kmn)}(h)+h^3\widehat{d}^{(mn)}\widetilde{H}_2^{(kmn)}(h)\right.$$
$$\left.\left.-2h\zeta^{(k)}\widetilde{J}_1^{(kmn)}(h)+4h^3\zeta^{(k)}\widetilde{J}_2^{(kmn)}(h)\right)\right\}\Big|_{k=m}^{k=n}$$

These expressions can be used to recover the stress field at the internal points of the domain.

4.3.7 Limit values of tractions (for hypersingular kernel)

To obtain the traction vector at the point x on the plane defined by the normal $(\underline{n}(x), n_{\mathbf{n}}(x))$, one can combine the stress components as follows (note that all vector and tensor components are given with respect to the local element coordinates):

$$\begin{aligned}\underline{t}(x) &= \underline{t}^{(\mathbf{p})}(x)+\underline{t}^{(\mathbf{n})}(x)\,n_{\mathbf{n}}(x) \qquad (21)\\ &= (\sigma_{11}(x)+\sigma_{22}(x))\,\underline{n}(x)+(\sigma_{11}(x)-\sigma_{22}(x)+i\sigma_{12}(x))\,\overline{n}(x)\\ &\quad +(\sigma_{13}(x)+i\sigma_{23}(x))\,n_{\mathbf{n}}(x)\\ t_{\mathbf{n}}(x) &= \sigma_{33}(x)\,n_{\mathbf{n}}(x)+\frac{1}{2}\overline{(\sigma_{13}(x)+i\sigma_{23}(x))}\underline{n}(x)+\frac{1}{2}(\sigma_{13}(x)+i\sigma_{23}(x))\,\overline{n}(x)\end{aligned}$$

To meet the boundary conditions, one should evaluate the limits of the above expressions as the field point x approaches some collocation point x' at the boundary. The evaluation of limits is straightforward for non-singular expressions (i.e. when the collocation point does not belong to the element). The evaluation of singular expressions that represent the influence of each element to the total traction on the same element is equivalent to taking the limits of tractions as $h \longrightarrow 0$. It could be done using the following relations:

$$
\begin{aligned}
r^{(k)} &\underset{h\longrightarrow 0}{\longrightarrow} \rho^{(k)} \\
\widetilde{G}_1^{(kmn)}(h) &\underset{h\longrightarrow 0}{\longrightarrow} \frac{\tan\chi^{(kmn)}}{\rho^{(k)}} = \frac{\sin\chi^{(kmn)}}{\left|d^{(mn)}\right|} \\
\widetilde{G}_2^{(kmn)}(h) &\underset{h\longrightarrow 0}{\longrightarrow} -\frac{\tan\chi^{(kmn)}}{\rho^{(k)}} = -\frac{\sin\chi^{(kmn)}}{\left|d^{(mn)}\right|} \\
\widetilde{G}_3^{(kmn)}(h) &\underset{h\longrightarrow 0}{\longrightarrow} -\frac{3}{2}\frac{\tan\chi^{(kmn)}}{\rho^{(k)}} = -\frac{3}{2}\frac{\sin\chi^{(kmn)}}{\left|d^{(mn)}\right|} \\
\widetilde{H}_1^{(kmn)}(h) &\underset{h\longrightarrow 0}{\longrightarrow} \frac{\sin\chi^{(kmn)}}{\left|d^{(mn)}\right|^2} \\
\widetilde{H}_2^{(kmn)}(h) &\underset{h\longrightarrow 0}{\longrightarrow} \frac{\sin\chi^{(kmn)}}{\left|d^{(mn)}\right|^4}\left(3-\sin^2\chi^{(kmn)}\right) \\
\widetilde{H}_3^{(kmn)}(h) &\underset{h\longrightarrow 0}{\longrightarrow} \frac{\sin\chi^{(kmn)}}{\left|d^{(mn)}\right|^6}\left(15-10\sin^2\chi^{(kmn)}+3\sin^4\chi^{(kmn)}\right)
\end{aligned}
\tag{22}
$$

The limit values of tractions (21) are as follows:

$$
\begin{aligned}
t_{\mathbf{n}}^{(\mathbf{n})}(x') &= \frac{\mu}{4\pi(1-\nu)}u_{\mathbf{n}} \sum_{\substack{m,n=1\\ n=(m+1)\bmod 3}}^{3} \frac{1}{\left|d^{(mn)}\right|}\sin\chi^{(kmn)}\Bigg|_{k=m}^{k=n} \\
\underline{t}^{(\mathbf{n})}(x') &= \frac{\mu}{4\pi(1-\nu)}\underline{u} \sum_{\substack{m,n=1\\ n=(m+1)\bmod 3}}^{3} \frac{(\nu-2)}{2\left|d^{(mn)}\right|}\sin\chi^{(kmn)}\Bigg|_{k=m}^{k=n} \\
&\quad -\frac{\mu}{4\pi(1-\nu)}\overline{u}\sum_{m,n=1}^{3}\frac{\nu}{2\left|d^{(mn)}\right|}\Big[\sin\chi^{(kmn)}(\cos 2\beta^{(mn)}+i\sin 2\beta^{(mn)}) \\
&\quad +2\cos^2\chi^{(kmn)}\left(\sin\beta^{(mn)}-i\cos\beta^{(mn)}\right)\left(\cos\varphi^{(kmn)}+i\sin\varphi^{(kmn)}\right)\Big]\Big|_{k=m}^{k=n} \\
\underline{t}^{(\mathbf{p})}(x') &= -\frac{\mu}{4\pi(1-\nu)}\underline{n}(x)\,u_{\mathbf{n}} \sum_{\substack{m,n=1\\ n=(m+1)\bmod 3}}^{3} \frac{(1+2\nu)}{2\left|d^{(mn)}\right|}\sin\chi^{(kmn)}\Bigg|_{k=m}^{k=n} \\
&\quad -\frac{\mu}{4\pi(1-\nu)}\overline{n}(x)\,u_{\mathbf{n}} \sum_{\substack{m,n=1\\ n=(m+1)\bmod 3}}^{3} \frac{(1-2\nu)}{2\left|d^{(mn)}\right|}\Big[\sin\chi^{(kmn)}(\cos 2\beta^{(mn)}+i\sin 2\beta^{(mn)}) \\
&\quad +2\cos^2\chi^{(kmn)}\left(\sin\beta^{(mn)}-i\cos\beta^{(mn)}\right)\left(\cos\varphi^{(kmn)}+i\sin\varphi^{(kmn)}\right)\Big]\Big|_{k=m}^{k=n}
\end{aligned}
\tag{23}
$$

where

$$
\begin{aligned}
\chi^{(kmn)} &= \arg z^{(k)} - \arg \underline{d}^{(mn)} \\
\beta^{(mn)} &= \arg \underline{d}^{(mn)} \\
\varphi^{(kmn)} &= \chi^{(kmn)} + \beta^{(mn)}
\end{aligned}
$$

Note that the first two of these expressions coincide with those obtained by Linkov and Mogilevskaya (1986) who fomulated a boundary hypersingular integral equation for a planar crack.

4.3.8 System of linear equations

The total traction $\mathbf{t}(x')$ could be obtained by summing up the contributions from all boundary elements represented by Eqs. (21) and (23). Before the summation, the stress tensor should be transformed to the "global" coordinate system using the rotation tensor R_ξ associated with the "local" element coordinate system (standard coordinate transformation). The system of equations is set up by the collocation method. The expessions for the tractions exactly represent the known values of those at the points that coincide with the centers of the boundary elements. This procedure results in the system of linear equations to determine the unknown displacement discontinuities $\mathbf{u}(\xi)$. The right-hand side of the system represents the boundary conditions for tractions and the specified far-field stress (load at infinity).

4.3.9 Postprocessing

The stress tensor components at any chosen point in the domain can be recovered using Eqs. (17) - (20) or, if necessary, their limit values, and substituting the calculated displacement discontinuities $\mathbf{u}(\xi)$. The particular interest is rather in calculation of the stress intensity factors, which determine the stability or the direction and rate of growth of cracks. At the present stage it is already possible to obtain those by using the distribution of the crack displacement discontinuity. However, the accuracy of the estimates may be insufficient, even with relatively fine mesh (see subsection 4.4). This issue is planned to be addressed by using the special approximations accounting for specific crack tip opening (or sliding) asymptotics (see subsection 5.2).

4.4 Validation

4.4.1 Comparison with existing benchmark results

The approach has been tested on a number of analytical and numerical benchmark problems. Those include

- the problem of a single penny-shaped crack in infinite medium subject to either normal or shear far-field stress,
- the plane strain problem of a half-circular crack in the infinite domain with biaxial far-field load.

The latter problem can be simulated by considering a three-dimensional crack shaped as a long half-cylinder with dimension in the axial direction much larger as compared to the other directions and loaded perpendicularly to its axis. The results for the benchmark problems as well as the comments on the reference solutions are given in the following subsections.

4.4.2 Penny-shaped crack

Since the main interest at this stage is in accurate calculation of the crack opening (or sliding) and the stress field, it would be useful to have some closed-form analytical solutions for both displacement discontinuities and stresses. The problem of a single planar crack of circular shape (penny-shaped crack) in an infinite elastic medium loaded in tension at infinity has been first solved analytically by Sack (1946) and Sneddon (1946). Green (1947) suggested an alternative method of solution by reducing the problem to an equivalent one for a axisymmetric harmonic potential. The solution of the analogous problem of a penny-shaped crack under shear loading was suggested by Segedin (1951). The closed-form expressions for the stresses in both loading cases ($\sigma_{zz} = S$ or $\sigma_{xz} = S$) can be found in the paper by Kachanov (1994). Fig. 4 shows an example of the meshes used in the numerical test performed with the present approach. Figures 5 (a) and (b) show the calculated displacement discontinuity (scaled by the factor $\frac{1}{4\pi(1-\nu)}$) components compared to the analytical solutions for the cases of normal and shear loading, respectively. Figures 6 and 7 show the stress tensor components (numerical vs. analytical solution) along two straight lines: $y = 0, z = 0.5a$ and $y = z = 0.5a$, where a is the radius of the crack.

From these plots one can see good agreement with the analytical results with accuracy increasing with the mesh density. However, near the crack tip the method accuracy is insufficient due to the use of constant approximations for displacement discontinuity.

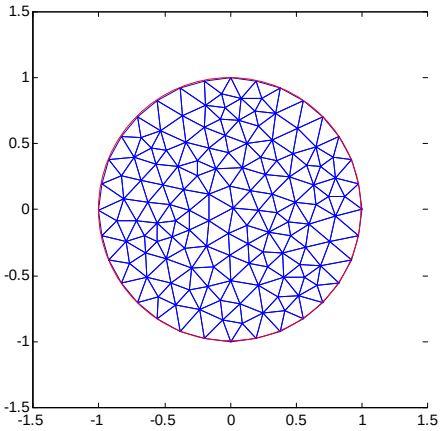

Figure 4: Boundary mesh for the penny-shaped crack problem

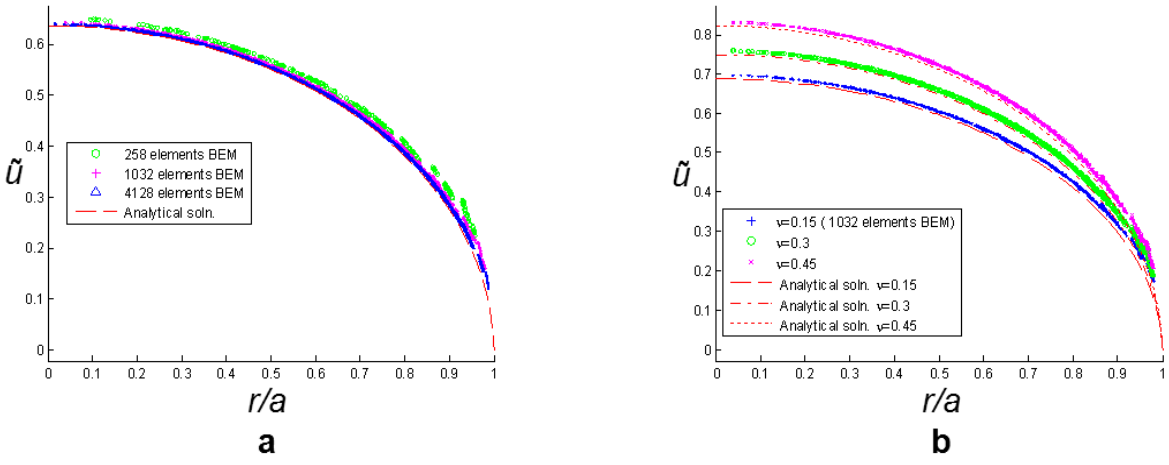

Figure 5: Scaled displacement discontinuity for a penny-shaped crack under normal (a) and shear (b) loading.

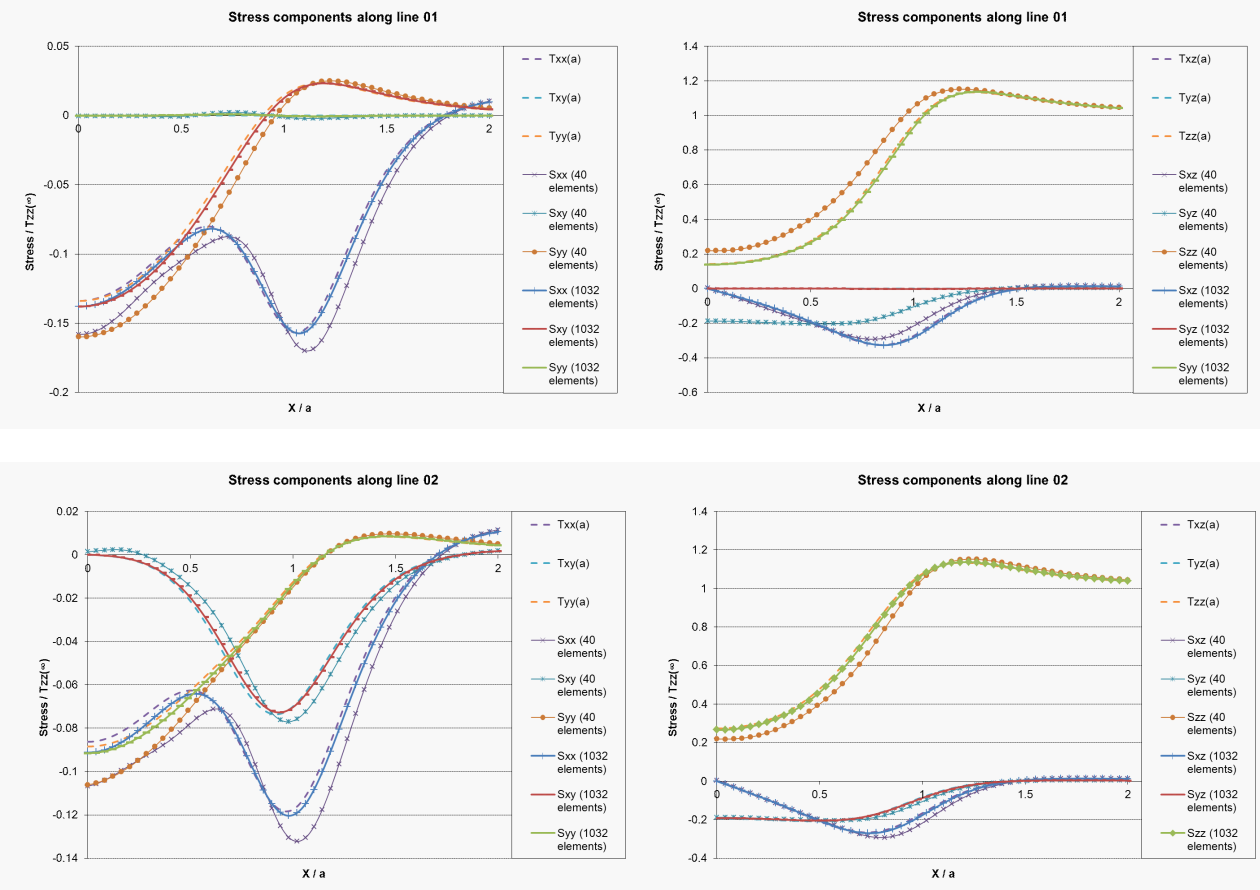

Figure 6: Stresses around a penny shape crack under normal tension. Comparison with the analytical solution.

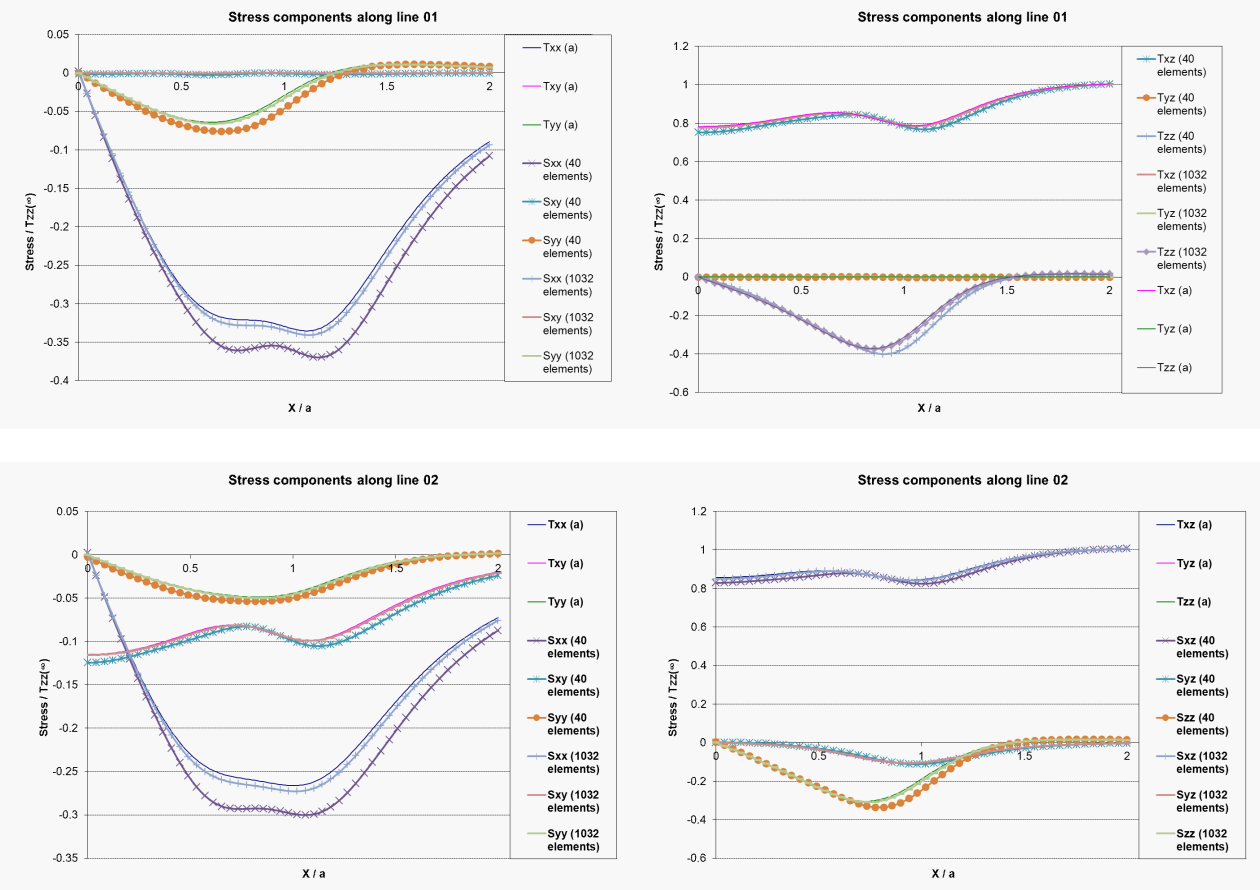

Figure 7: Stresses around a penny-shaped crack under shear. Comparison with the analytical solution.

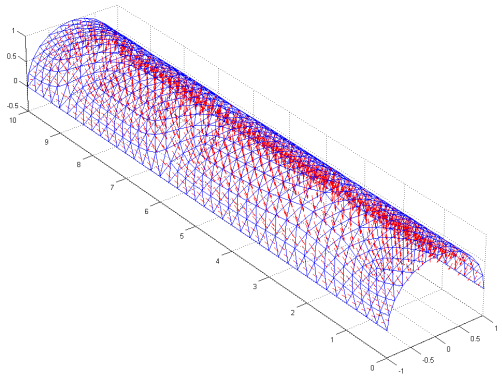

Figure 8: The boundary mesh and the evaluated displacement discontinuities for a semi-cylindrical crack.

4.4.3 Plane strain problems

Consider the two-dimensional plane strain problem of a semi-circular crack in an infinite medium under biaxial tension at infinity. This problem can represent an approximate solution (in the appropriate cross-section) of the three-dimensional problem of a long semi-cylindrical crack loaded in the directions perpendicular to the axis of the cylinder (see Fig. 8).

The analytical solution for the corresponding plane strain problem can be found in the book by Muskhelishvili (1963).

Fig. 8 shows the mesh used in the three-dimensional test performed with the present approach as wellas the calculated displacement discontinuity vectors at the collocation points. Fig. 9 shows the stress field (stress components along different straight lines) in the middle cross-section ($y = 0.5L$, where $L = 10a$ is the crack length, a is the curvature radius) compared to the plane strain solution.

5 Future work

5.1 Higher order approximations

BEM provides stable results even with the simplest piecewise-constant approximations of unknowns. Hovever, to improve accuracy, large number of elements is required and, consequently, the computational cost could be high. To reduce this cost, quadratic approximations of unknowns are planned to be introduced. In this procedure, analytical integration can still be used. In fact, all integral terms involved in the present (constant approximation) scheme will still be included in the final expressions for quadratic approximations. Additional integrals related to the higher order terms are expected to be handled analytically.

5.2 Crack tip elements

Although stress intensity factors can be estimated using constant approximations for the unknowns, those estimtes would lack the required accuracy. Accurate treatment of the crack front singularities requires the implementation of specific shape functions for the unknowns on the elements adjacent to the crack front. It is well known that the leading terms in the power series expansion of the displacement discontinuity on the crack near its front are proportional to $\sqrt{r}$, where r is the distance from the crack front. For the stress components, the leading term is proportional to $1/\sqrt{r}$. This leads to the idea of including an additional multiplier of $\sqrt{r}$ in the approximating (shape) functions for the displacement discontinuity at the elements adjacent to the crack front. Additional integrals that include the crack front approximations are again expected to be handled analytically.

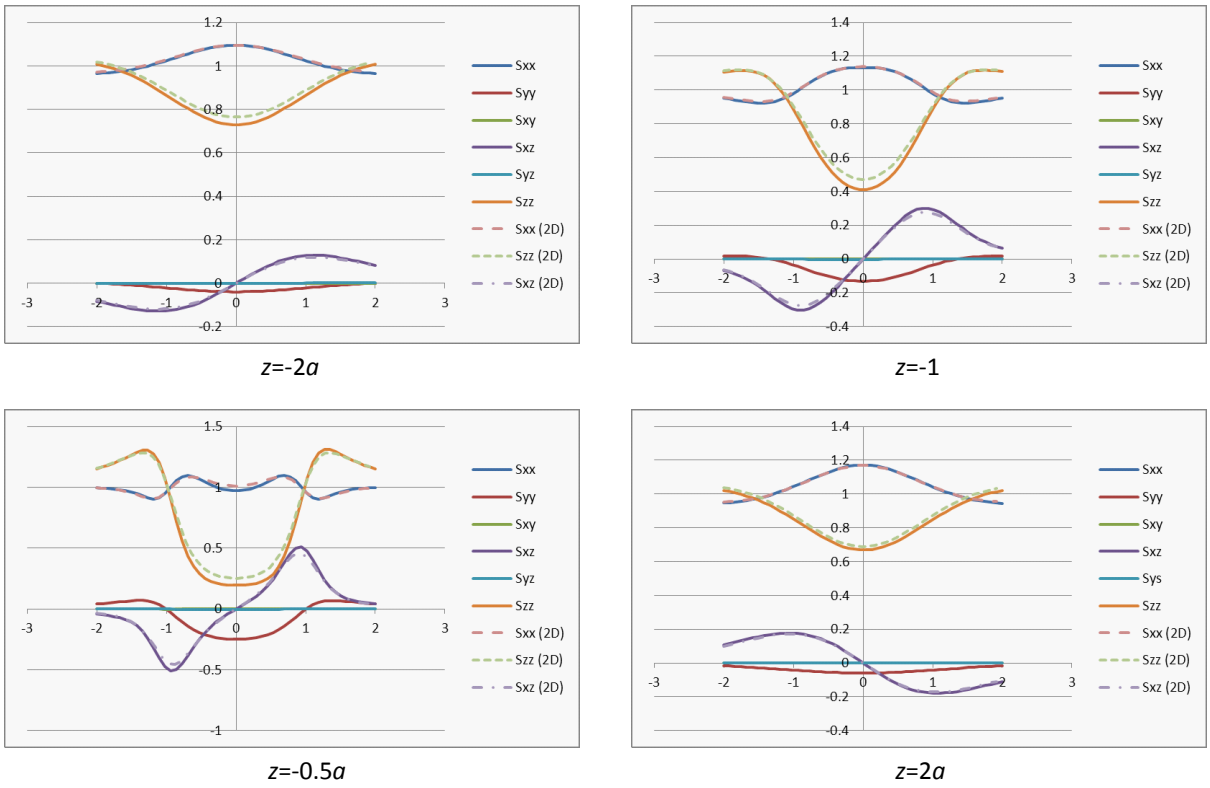

Figure 9: Stresses in the central cross-section of a semi-cylindrical crack under biaxial tension. Comparison with plane strain results.

5.3 Treatment of inhomogeneities

Inhomogeneities can be described using standard Multi-region formulation (see Aliabadi 2002). In this formulation, the system of boundary equations for each subdomain (including inhomogeneities) are supplemented by the boundary conditions for the interfaces between the subdomains (e.g. perfect bond). Then various techniques to efficiently assemble the final system of linear equations will be analyzed and implemented.

5.4 Treatment of body forces

Body forces involved in the described formulation are assumed constant for each subdomain (inhomogeneity or the rock matrix), which may not be the general case. In general, the techniques such as Dual Reciprocity Method (see Gaul et al. 2003) could be used to reduce the volume integrals to the boundary ones. However, it is planned to explore different approaches including that based on the representation of the body forces via a set of vector spherical harmonics.

5.5 Modelling crack propagation

The approach developed up to date can be used in straightforward manner to model quasistatic crack propagation. The present elastostatic model can be used on each step in combination with the appropriate crack propagation criteria. Various criteria are available (see e.g. Meng et al., 2013); it is planned to explore and analyze those criteria for further use in crack growth simulations.

References

[1] Aliabadi, 2002. The Boundary Element Method. Vol.2. Wiley, New York

[2] Barber, J.R. 2010. Solid mechanics and its applications: Elasticity. Springer Science, London, New York

[3] Bui, H.D. 1977. An integral equations method for solving the problem of a plane crack of arbitrary shape. J.Mech.Phys.Solids, 25 (1), 29-39

[4] Chen, B. and Gross, D. 1997. Two parallel penny-shaped cracks under the action of dynamic impacts. Archive of Applied Mechanics 67, 555-565

[5] Chen, Y.Z. and Lee, K.Y. 2001. Numerical solution of three-dimensional crack problem by using hypersingular integral equation. Comp.Meth.Appl.Mech.Engng. 190 (31), 4019-4026

[6] Crouch, S.L. 1976. Solution of plane elasticity problems by the displacement discontinuity method. Int.J.Numer.Meth.Engng. 10, 301-343

[7] Cruse, T.A. 1988. Boundary Element Analysis in Computational Fracture Mechanics. Kluwer academic publishers, Dordrecht, Boston, London

[8] Fabrikant, V.I. 1987. Penny-shaped crack revisited: closed-form solutions. Phil.Mag.A. 56 (2), 191-207

[9] Frangi, A., Novati, G., Springhetti, R., Rovizzi, M. 2002. 3D fracture analysis by the symmetric Galerkin BEM. Comp.Mech. 28, 220–23

[10] Gaul, L., Koegl, M., and Wagner, M. 2003. Boundary Element ethods for Engineering Applications. Springer-Verlag, Berlin, Heidelberg, New York

[11] Gradshteyn, I.S. and Ryzhik, I.M. 19. Table of Integrals, Series, and Products, sixth edition. Academic press, San Diego, San Francisco, New York, Boston, London, Sydney, Tokyo

[12] Gray, L.J. 1990. Hypersingular integrals in boundary element fracture analysis. Int.J.Numer.Meth.Engng. 29, 1135-1158

[13] Green, A.E 1949. On Boussinesq's problem and penny-shaped cracks. Math.Proc.Cambridge Phil.Soc. 45 (2), 251-257

[14] Kachanov, M. 1994. Elastic solids with many cracks and related problems. Adv.Appl.Mech. 30, 259-445

[15] Kolk, K., Weber, W., and Kuhn, G. 2005. Investigation of 3D crack propagation problems via fast BEM formulations. Comp.Mech. 37 (1), 32-40

[16] Kuriyama, k. and Mizuta, Y. 1993. Three-dimensional elastic analysis by the Displacement Discontinuity Method with boundary division into triangular leaf elements. Int.J.Rock Mech.Min.Sci.&Geomech.Abstr. 30 (2), 111-123

[17] Kushch, V. 1998. Interacting cracks and inclusions in a solid by multipole expansion method Int.J.Solids Struct. 35 (15), 1751-1762

[18] Kushch, V. and Sangani, A.S. Stress intensity factor and effective stiffness of a solid containing aligned penny-shaped cracks. Int.J.Solids Struct. 37. 6555-6570

[19] Lachat, J.C., Watson, J.O. 1976. Effective numerical treatment of boundary integral equations: a formulation for three-dimensional elastostatics. Int J Num Meth Eng 10, 991-1005

[20] Lin'kov and Mogilevskaya, S.G. 1986. Finite-part integrals in problems of three-dimensional cracks. J.Appl.Math.Mech. 50 (5), 652-658

[21] Liu, Y. 2009. Fast Multipole Boundary Element Method - Theory and Applications in Engineering. Cambridge university Press.

[22] Lo, S.H., Dong, C.Y., and Cheung, Y.K. 2005. Integral equation approach for 3D multiple-crack problems. Eng Fract.Mech 72 (12), 1830-1840

[23] Luchi and Rizzuti 1987. Boundary elements for three-dimensional elastic crack analysis. Int.J.Numer.Meth.Engng. 24, 2253-2271

[24] Meng, C., Maerten, F., and Pollard, D. D. 2013. Modeling mixed-mode fracture propagation in isotropic elastic three dimensional solid. Int.J.Fract. 179, 45-57

[25] Mi, Y. and Aliabadi, M.H. 1994. Three-dimensional crack growth simulation using BEM. Computers and Structures, 52 (5), 871-878

[26] Milroy, J. Hinduja, S., and Davey, K. 1997. The elastostatic three-dimensional boundary element method: analytical integration for linear isoparametric triangular elements. Appl.Math.Modelling, 21, 763-782

[27] Muskhelishvili, N.I. 1963. Some Basic Problems of the Mathematical Theory of Elasticity - fundamental equations, plane theory of elasticity, torsion, and bending. P.Noordhoff, Groningen

[28] Nintcheu Fata, S. 2011. Explicit expressions for three-dimensional boundary integrals in linear elasticity. J.Comp.Appl.Math. 235, 4480-4495

[29] Sack, R.A. 1946. Extension of Griffith's theory of rupture to three dimensions. Proc.Phys.Soc.London. 58, 729

[30] Salvadori, A. 2001. Analytical integrations of hypersingular kernel in 3D BEM problems. Comput.Meth.Appl.Mech.Engrg. 190, 3957-3975

[31] Segedin, C.M. 1951. Note on a penny-shaped crack under shear. Math.Proc.Cambridge Phil.Soc. 47 (2), 396-400

[32] Sneddon, I.N. 1946. The distribution of stress in the neighbourhood of a crack in an elastic solid. Proc.Roy.Soc. A. 187, 229

[33] Watson, J.O. 2005. Boundary elements for cracks and notches in three dimensions. Int.J.Numer.Meth.Engng. 65, 1419-1443

[34] Weaver, J. 1977. Three-dimensional crack analysis. Int.J.Solids Struct. 13 (4), 321-330

[35] Wrobel, L.C. 2002. The Boundary Element Method. Vol.1. Wiley, New York